Available online at www.sciencedirect.com
SCIENCE DIRECT®
Journal of Computational Physics 189 (2003) 390–426
JOURNAL OF COMPUTATIONAL PHYSICS
www.elsevier.com/locate/jcp

Fragmentation, merging, and internal dynamics for PIC simulation with finite size particles

Dennis W. Hewett

AX-Division, Lawrence Livermore National Laboratory, Livermore, CA 94550, USA

Received 10 July 2002; received in revised form 17 March 2003; accepted 18 March 2003

Abstract

Components of a new type of "smart PIC" algorithm, intended to bridge the gap between Eulerian fluid regimes and kinetic regimes, are developed. Enlarging the scope of PIC, the CPK method (Complex Particle Kinetic) concept uses an ensemble of small, fluid-like macro-particles to represent particle distributions in phase space. These macro-particles are Gaussian-shaped in both position and velocity compared to the phase-space delta functions used in standard PIC and the spatial "sugar cube" particles used in an early version of this model [1]. Time evolution is modeled by a combination of the Lagrangian motion and internal evolution within each individual macro-particle. An analytic term is added to each particle's shape that represents internal evolution consistent with the collisionless, free-streaming of each macro-particle. Collision-dominated, γ-law gas internal evolution is also developed to define the opposite limit of collisionality. Similar to our initial effort, macro-particles are aggressively fragmented in phase space to probe for emerging kinetic features and aggressively merged, for economy, if interesting features fail to materialize. With CPK, fragmentation in both position and velocity space can be accomplished without loss of significant phase space information. Fragmentation preserves the kinetic capabilities of PIC; merging dramatically shrinks the number of particles in non-kinetic or collisional regions. In collision-dominated regimes, merging naturally produces a few Lagrangian particles that act much as nodes in Free-Lagrangian hydrodynamics. The only interaction between neutral particles is through merging; no mesh-dependent pressure gradients are needed. Finally, a linked-list data structure significantly reduces time spent "sorting" nearest neighbors for potential merging—and should lead to straightforward MPP operation.

1. Introduction

In plasma or rarified gas physics, collisions are rare but often non-ignorable events. To model systems with arbitrary collisonality, it is first necessary to build a model that is fully capable of capturing collisionless, kinetic behavior. As collisions become more frequent, this ideal model would progress smoothly

E-mail address: hewett1@llnl.gov.

0021-9991/$ - see front matter
doi:10.1016/S0021-9991(03)00225-0

and continuously from collisionless particle dynamics to collision-dominated fluid. Such an ideal model, valid in all parameter regimes, has yet to be developed.

In the high-density, collision-dominated limit, the essential physics is well captured by the Eulerian fluid equations. The tacit assumption of this fluid model is that underlying velocity representation is a simple Maxwellian, with a non-zero-center location to represent macroscopic drift and a non-uniform half-width to represent spatial temperature variations of the fluid. The relative simplicity obtained with this velocity representation is often exploited by adding geometric complexity to the spatial representation, frequently by letting the mesh move with the fluid. Such Lagrangian motion of the computational mesh is widespread in the computational design of complex systems. Additional terms can be added to extend the utility of these models (Navier–Stokes equation) some small distance into the viscous or long mean-free-path regime, but these additions fall far short of the rarified gas regime.

On the other extreme, Particle-In-Cell (PIC)/Monte Carlo (MC) techniques have been used for years by representing arbitrary distributions of real particles in phase space by grouping them together in self-similar clumps of macro-particles. Starting from early methods attempting to recover fluid flow [2,3], PIC has enjoyed widespread use, particularly, in collisionless, electromagnetic plasma physics applications [4,5]. The tradeoff for this detailed description of the physics is that the model domain becomes very microscopic for many applications. Only with the advent of modern computing capacity has PIC/MC been capable of more than modest geometric complexity. Most often in plasma physics, a reduced fluid-like description is still used to eliminate high frequency electron behavior in order to focus computational effort on ion dynamics [6]. (Consider the difference between oscillation frequencies of the electron to that of a singly ionized Cesium ion, for example.) The addition of discrete collisionality, adding significantly to both the complexity and CPU requirements of the algorithm, stretches the model some small distance toward the collision-dominated fluid regime.

Clearly, there is a large gap in our modeling capability between the kinetic and fluid regime. Many have noticed this gap. Coming from the fluid limit, the standard approach is to add Navier–Stokes terms for viscous effects [7,8]. From the other direction, Takizuda and Abe [9] describe a binary collision model for PIC that has become a standard. Birdsall [10] describes the PIC–MC scheme as a means to add chemistry and ionization to the PIC scheme. Rambo and Denavit [11] and later Rambo and Procassini [12] present detailed comparisons between PIC and fluid descriptions. Jones et al. [13] discuss a grid-based collision model based on building a distribution from the particles then colliding each individual particle with this overall distribution. Hudson and Bartel [14] discuss state-of-the-art Direct Simulation Monte Carlo techniques applied to plasmas and rarified gases used in semiconductor manufacturing.

Impressive gains have recently materialized in related areas. Both Adaptive Mesh Refinement (AMR) and Arbitrary Lagrangian Eulerian (ALE) fluid codes provide significant economies by introducing high-resolution spatial meshes only in regions of high ''activity''. The AMR method [15] does this using Richardson refinement in such regions while the ALE method [16] has a Lagrangian mesh that moves with the flow of some macroscopic quantity (usually the mass density) thereby automatically bringing mesh points into interesting regions of convergence. The ''E'' part of ALE comes in when some amount of an Eulerian description allows enough fluid flow through the mesh to prevent complicated flows from tangling the mesh. Particle methods avoid this problem since these methods have no essential mesh that can tangle. Smooth Particle Hydrodynamics (SPH) [17] is an intriguing extension of these ideas that shows great promise for certain types of fluid/solid interactions. However, even if granted complete success, the best one can obtain from these models is collision-dominated fluid physics.

The adaptive spatial resolution concept is also useful in reducing the expense of kinetic PIC/MC modeling in the partially collision regime. The particle noise in these models is directly related to the number of particles per spatial mesh point/cell, regardless of the cell size. If the spatial resolution can be decreased in certain areas, then the total number of particles required diminishes as well.

As important as the improvements derived from adaptive meshes have been, we are still far short of the necessary capability in the collisional regime. Brute force is still required and, even with the most remarkable gains in modeling capability arising from Moore's law, simulations with still-inadequate models run for weeks at a time. A first step towards a more capable model was the Blob method by Coppa et al. [18]. The Blob concept uses particles whose size could stretch in response to electromagnetic field gradients across the finite size particle. A different approach, and the precursor to this work, is the Grid and Particle Hydrodynamics (GaPH) model proposed by Bateson and Hewett [1]. The key concept in adaptivity used in GaPH is to add resolution and then check to see if the additional resolution significantly changes the physics. The GaPH model adds such resolution by aggressively generating new particles to probe for emerging features and aggressively merging particles if interesting features fail to materialize. A key feature was that the extra freedom now built into each particle has the essential feature of a Maxwellian velocity distribution. Thus, the GaPH algorithm used the adaptive concept in both space and velocity. Further, as collisionality increases and correspondingly diminishes the non-Maxwellian features of the particle distribution, the easier it is for a small number GaPH particles to represent the distribution.

What is presented here is the next step beyond the GaPH algorithm. To make an algorithm truly adaptive we must have the ability to increase the resolution without changing or adding any physics. Given a phase space distribution approximated to some degree of fidelity by a collection of particles, first we increase the resolution without changing the degree of fidelity of the approximation. Following the subsequent time step, we may find that the increased resolution has produced a significantly different distribution. It is these changes we wish to preserve. However, it is crucial that the act of increasing the resolution itself does not change the physics. If the increased resolution does change the physics, the task of merging uninteresting physics becomes more subjective: one of preserving what we have trained the algorithm to expect rather than preserving the physics that emerges from the underlying equations.

The new algorithm presented here, called CPK for Complex Particle Kinetics, begins with a substantially different basic particle. The new "particle" has generally the form of a Gaussian distribution in all phase-space directions. An arbitrary distribution of real particles can be made as a superposition of these "particles". One of the key capabilities is the ability to fragment each particle in a way that will not introduce new physics. With this procedure we can replace each particle with a set of particles that, when reassembled, give the original particle to arbitrary precision. Further, with some time-dependent built into each particle, fragmentation is not required to preserve existing details during time evolution. Collisionless, free expansion of an isolated puff of gas can be followed by a single macro-particle with no fragmentation, if necessary. The redundancy introduced by the fragmentation provides the freedom to represent new features emerging from the nonlinear time evolution. In addition to collisionless internal particle dynamics, we have also developed internal dynamics consistent with a γ-law gas within each particle. This ability, coupled with a very aggressive strategy for merging particles with disparate velocities, puts full fluid behavior within reach.

Another part of the CPK concept is that the physics unfolds as nature intends. The only connection between neutral particles is through collisions, for the moment only through (perhaps aggressive) merging. The gradient of pressure is not computed and the "mesh" enters only in a non-fundamental way as a means to facilitate evaluating particle "overlap" in phase space in preparation for merging. The mesh never carries any essential part of the physics; the mesh could be discarded every time step if, for some reason, a new one offered some advantage.

In the next section, we will discuss the new CPK basis particle, surrounded and followed by restatement and expansion of the finite size particle concept and mechanics. Next, will be a presentation of some early results in both the kinetic and full-fluid limit, followed by discussion and conclusions.

2. The CPK macro-particle

2.1. The basic CPK particle shape with velocity shear

The fundamental element of the CPK concept is the macro-particle. This particle is a collection of real particles that have a Gaussian spatial profile about the central macro-particle Lagrangian location and that have a Maxwellian velocity profile about the Lagrangian drift, the average of the velocities of the real particles in each macro-particle. Each CPK macro-particle carries the phase-space information for the real particles it represents through the functional form

$$f(\vec{x},\vec{v}) = \frac{W_{8o}}{(2\pi)^3 w_{dox} w_{doy} w_{doz} v_{tox} v_{toy} v_{toz}} \exp\left\{ -\left[\frac{\left(\vec{x}-\vec{x}_o\right)^2}{2\vec{w}_{do}^2} + \frac{\left(\vec{v}-\vec{u}_d\right)^2}{2\vec{v}_{to}^2} \right] \right\} \tag{2.1.1}$$

in which W_{8o} is the number of real particles, $\vec{w}_{do}$ is the half-width in each space direction and $\vec{v}_{to}$ is the thermal velocity (velocity half-width), and $\vec{x}_o$ and $\vec{u}_d$ are the location and drift of the basic CPK particle.

Such particles will be the basis set from which the total distribution of real particles can be constructed by superposition. It is assumed that an arbitrary distribution of real particles can be represented by such a superposition, at least as well as could be done with the traditional PIC/MC delta functions and their associated "shape factors". Like its predecessor, GaPH [1], these particles are each Maxwellian in velocity, a property that will be useful for particle consolidation as collisonality relaxes the composite distribution towards a Maxwellian.

The spatial coordinates have the same functional form as the velocity coordinates. Although a "Maxwellian" in space does not have the same physics implications as a Maxwellian in velocity, the similarity in representation for these independent coordinates will be very useful in phase-space operations. Even with this basic CPK particle definition, this spatial dependence is no more objectionable than the traditional PIC/MC representation. An obvious difficulty is initializing configurations with "sharp" discontinuities with these broad Gaussian-shaped particles. These discontinuities will be at least as wide as the spatial half-width of the macro-particles that represent this density. We will show that such discontinuities can sharpened using particle fragmentation options, as is shown in one of the applications (Section 3.2).

A simple generalization of the basic particle shape (2.1.1) allows even more flexibility. We add another piece to the spatial part of the exponential in the basic particle shape to account for internal time evolution. To see this, consider the time evolution of the distribution of real particles, grouped together in an isolated CPK particle, shown in 1-D phase space in Fig. 1(a). In the absence of collisions and forces, each real particle that has a velocity greater than the CPK particle drift will move to the right of the CPK center. Conversely, those with a velocity less than the average will move towards the left—simply the physics of free-expansion.

In a probabilistic interpretation of the distribution function, each particle transports a piece of the distribution function along its characteristic orbit. In this case, the orbit is a simple straight line given by

$$\vec{x} = \vec{x}_{\tau=0} + \left(\vec{v}-\vec{u}_{\tau=0}\right)\tau.$$

Thus, those particles that contribute to a Gaussian spatial profile in each small interval in velocity space can drift with respect to the rest of the macro-particle. The advanced distribution function, generalized to 3-D, can be expressed by adding this drift explicitly into the spatial argument in (2.1.1) to get

$$f(\vec{x},\vec{v}) = \frac{W_{8o}}{(2\pi)^3 w_{dox} v_{tox} w_{doy} v_{toy} w_{doz} v_{toz}} \exp\left\{ -\left[\frac{\left[\vec{x}-\vec{x}_o-\left(\vec{v}-\vec{u}_d\right)\vec{\tau}\right]^2}{2\vec{w}_{do}^2} + \frac{\left(\vec{v}-\vec{u}_d\right)^2}{2\vec{v}_{to}^2} \right] \right\} \tag{2.1.2}$$

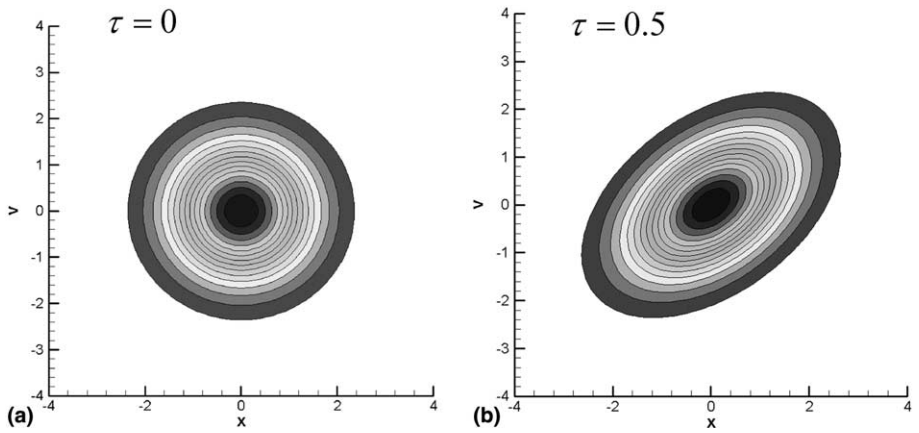

Fig. 1. (a) The basic CPK particle form at $\tau = 0$. (b) The same particle after a finite time τ. Note that, consistent with free expansion, there is no increase in velocity of any contour; the macro-particle has simply sheared in space.

where the new contribution depends explicitly on an internal evolution time $\bar{\tau}$ and is proportional to the difference between an individual real particle's velocity and the CPK mean velocity. Note that the time may be different in each spatial direction; the vector notation implies

$$\frac{\left[\vec{x}-\vec{x}_o-\left(\vec{v}-\vec{u}_d\right)\bar{\tau}\right]^2}{2\vec{w}_{do}^2}+\frac{\left(\vec{v}-\vec{u}_d\right)^2}{2\bar{v}_{to}^2}=\frac{\left[x-x_o-(v_x-u_{dx})\tau_x\right]^2}{2w_{dox}^2}+\frac{(v_x-u_{dx})^2}{2v_{tox}^2}+\frac{\left[y-y_o-\left(v_y-u_{dy}\right)\tau_y\right]^2}{2w_{doy}^2}+\frac{\left(v_y-u_{dy}\right)^2}{2v_{toy}^2}+\frac{\left[z-z_o-(v_z-u_{dz})\tau_z\right]^2}{2w_{doz}^2}+\frac{(v_z-u_{dz})^2}{2v_{toz}^2}. \tag{2.1.2a}$$

Shown in Fig. 1(a) is a particle at zero time and in Fig. 1(b) is the same particle after a finite time τ_x. Since each CPK particle can now analytically capture-free expansion, the entire distribution of real particles represented by the superposition CPK particles will also have this ability.

2.2. Fragmentation in velocity

It is clear that we intend to fragment macro-particles for the increased resolution needed to probe for emerging features. It is essential that the fragmentation process itself not add new features. This problem can be avoided by splitting each CPK particle into pieces constructed so that the new particles reproduce the original particle when added together. If the sum of the parts of each CPK particle is invariant to the fragmentation process, the superposition of all CPK particles representing the total distribution will also be invariant. The procedure that we now present accomplishes this goal very effectively.

The fragmentation concept is based on the conservation laws that are required for each CPK particle. Consider a 1-D version of a CPK particle split into a middle particle and two "probe" particles in velocity. Since the probe particles have equal mass and will be given equal and opposite drift increments relative to the drift of the original particle, linear momentum will be automatically conserved. Conservation of mass and energy will provide constraints useful for determining the properties of the new three-particle system. Doing the required integrals over velocity, the following conservation laws must be satisfied:

$$\text{mass:} \qquad W_{8o} = W_{8m} + 2W_{8p}, \tag{2.2.1}$$

$$\text{energy:} \qquad W_{8o}\left[v_{tox}^2 + u_{dx}^2\right] = W_{8m}\left[v_{tmx}^2 + u_{dx}^2\right] + W_{8p}\left[v_{tpx}^2 + \left(u_{dx} - u_{px}\right)^2\right] + W_{8p}\left[v_{tpx}^2 + \left(u_{dx} + u_{px}\right)^2\right]. \tag{2.2.2}$$

In these expressions, the subscripts m and p represent the "middle" and "probe" particles, respectively.

The resulting system has five unknowns, $W_{8m}, W_{8p}, v_{tmx}, v_{tpx}, u_{px}$, and these two equations. More equations are needed. Many options have been tried, ranging from the simple conservation of distribution values at specific points in velocity and space to complicated schemes to conserve entropy $\{\int \mathrm{d}x\,\mathrm{d}v f \ln(f)\}$. The most common failure of these schemes is that the new particle parameters are not sufficiently constrained to reproduce the distribution contained in the original particle when the new particle distributions are added together. Some concepts were rejected when it became clear that the resulting system of equations were too complicated to be practical.

A compromise between fidelity and complexity is to use an equation for the lowest velocity moment not yet conserved—the "one-sided" velocity moment. Consider the first moment of velocity integrated from the velocity center (in center of mass coordinates) of a probe particle 0 to $+\infty$. Consider first the integral for the $p+$ particle (that probe particle created slightly faster than the original).

$$B_{p+} = \frac{W_p}{2\pi w_{dx} v_{tpx}} \int_0^\infty \mathrm{d}v\, v \exp\left[-(v - u_{dx})^2/2v_{tpx}^2\right] b_{p+}(v),$$

$$b_{p+}(v) = \int_{-\infty}^{\infty} \mathrm{d}x \exp\left[-(x - x_o - (v - u_{dx})\tau)^2/2w_{dx}^2\right].$$

Similar expressions for all three particles can be evaluated and substituted into the conservation equation $B_o = B_m + B_{p-} + B_{p+}$ which leads to

$$\frac{W_{8o} v_{tox}}{\sqrt{2\pi}} = \frac{W_{8m} v_{tmx}}{\sqrt{2\pi}} + W_{8p}\left[\frac{v_{tpx}}{\sqrt{2\pi}} \exp\left(-u_{dx}^2/2v_{tpx}^2\right) - \frac{u_{dx}}{2}\,\mathrm{erfc}(+u_{dx}/\sqrt{2}v_{tpx})\right] + W_{8p}\left[\frac{v_{tpx}}{\sqrt{2\pi}} \exp\left(-u_{dx}^2/2v_{tpx}^2\right) + \frac{u_{dx}}{2}\mathrm{erfc}(-u_{dx}/\sqrt{2}v_{tpx})\right].$$

Using symmetries in the error function, this reduces to

$$W_{8o} v_{tox} = W_{8m} v_{tmx} + W_{8p}\left[2v_{tpx} \exp\left(-u_{dx}^2/2v_{tpx}^2\right) + \sqrt{2\pi} u_{dx} \mathrm{erf}(u_{dx}/\sqrt{2}v_{tpx})\right]. \tag{2.2.3}$$

Although (2.2.3) represents a quantity not usually expected to be conserved, the conservation of the one-sided velocity moment adds an important piece in the effort to preserve the distribution. Conserving this quantity helps prevent the situation that might occur if the middle particle were cold and the two probe particles were relatively hot—leading to a combination that, while satisfying energy, mass, and momentum conservation, gives a composite particle that has a cold peak with very broad "wings" on the velocity profile. We require that the sum of the three new particles give a velocity profile very similar to the original simple Maxwellian of the original particle.

To carry out the velocity fragmentation, values for the five unknowns, $W'_{8m}, W'_{8p}, v'_{tmx}, v'_{tpx}$, and u'_{px}, need to be determined given only three Eqs. (2.2.1)–(2.2.3). (The primes signify normalization to the weight W_{8o} and thermal velocity V_{to} of the original particle, as appropriate.) With more unknowns than equations, values may be assigned for two of the unknowns. Considering the complexity of the term in brackets in (2.2.3), a great choice is to pick u'_{px}, and v'_{tpx} so the difficult terms in the bracket become a simple constant to be

evaluated and used to solve for the remaining three unknowns. (The spatial widths of all three fragments remain equal to that of the original.)

Choosing u'_{px}, and v'_{tpx} ($\alpha \equiv u'_{dx}/v'_{tpx}$), coupled with the following definitions $\beta_1 \equiv 2v'_{tpx}\exp(-\alpha^2/2) + \sqrt{2\pi}u'_{dx}\mathrm{erf}(\alpha/\sqrt{2})$ and $\beta_e \equiv 2v'^2_{tpx}[1+\alpha^2]$, we obtain the following equations:

$$W'_{8p} = (2\beta_1 - 2 - \beta_e)/(\beta_1^2 - 2\beta_e) \qquad \text{(energy)}, \tag{2.2.4}$$

$$W'_{8m} = 1 - 2W'_{8p} \qquad \text{(mass)}, \tag{2.2.5}$$

$$v'_{tmx} = (1 - W'_p\beta_1)/W'_{8m}, \qquad \text{(1-sided momentum)}. \tag{2.2.6}$$

Unfortunately, there is no way to guarantee that the selections for u'_{px}, and v'_{tpx} lead to reasonable values for W'_{8m}, W'_{8p}, and v'_{tmx}. An acceptable way to proceed in this now smaller state space is to look at these three values while stepping through reasonable values for u'_{px}, and v'_{tpx}. None of the three computed values can be negative or greater than 1. For example, small u'_{px} values give $W'_{8m} > 1$, which, with increasing v'_{tpx}, become <1 just as v'_{tmx} becomes greater than 1. Tabulating the solutions of these equations quickly leads to good strategies for choosing u'_{px}, and v'_{tpx}. Shown in Table 1 are ranges of useful u'_{px} values for four reasonable values of v'_{tpx}.

W'_{8p} is not listed because it is trivially related to W'_{8m}. The ratio of W'_{8m}/v'_{tmx} is listed because, when greater than 1, the middle particle that is "taller" than the original, making it impossible to recover the original particle by summation. Notice also that there are no solutions for probe particles with less than $v'_{tpx} < .5$ or $v'_{tpx} > 1$—showing, surprisingly, that a probe particle that is hotter than or substantially colder than the original cannot be generated with this method.

The table lists but a few of the many possibilities. One interesting case, denoted by the *, uses $u'_{px} = 0.8$ and $v'_{tpx} = 0.8$ to produce nearly equal masses for the middle and probe particles. Another case, denoted by the &, uses $u'_{px} = 1.0$ and $v'_{tpx} = 0.8$ to produce a middle particle nearly equal in temperature to the probes. In this instance, the middle particle gets $\sim$2/3 of the original particle's mass.

Fragmentation based on this procedure is shown in Figs. 2 and 3. Using these parameters for the * case produces, from the original particle (a), a middle particle (b) and the two probe particles shown in (c). Shown in (d) is the sum of (b) and (c), which returns a composite particle whose L2 norm $\{= \int \mathrm{d}x\,\mathrm{d}v(f_{\mathrm{orig}} - f_{\mathrm{comp}})^2\}$ is within 0.5% of the original. Even though all particles retain the same velocity shear τ, the new particles are colder and thus appear to have aged so that they can be nestled together within the dashed ellipse that represents the footprint of the original particle. For this * case, the particles all have nearly equal masses and the middle particle is slightly cooler than each of the probe particles.

Had even more degrees of freedom been built into the basic particle shape, presumably the fit could be even better. However, this procedure for fragmentation does preserve the total mass, the momentum, the energy and one- sided velocity moment. The composite particle (d) is a fraction of a percent taller than the original (a) and slightly less elongated in the principal axis of the "footprint" ellipse. More judicious use of Table 1, or the equations that produced it, could further reduce this discrepancy, if required.

Finally, we note that for a velocity split, energy conservation is expressed by

$$W_{8o}v^2_{tox} = W_{8p}\left[v^2_{tpx} + u^2_{px}\right] + W_{8m}\left[v^2_{tmx}\right] + W_{8p}\left[v^2_{tpx} + u^2_{px}\right].$$

The conservation of the second spatial moment $\langle x^2\rangle$ takes the form

$$W_{8o}\left(w^2_{dox} + v^2_{tox}\tau^2_x\right) = W_{8m}\left[w^2_{dox} + v^2_{tmx}\tau^2_x\right] + 2W_{8p}\left[w^2_{dox} + v^2_{tpx}\tau^2_x + x^2_p\right].$$

Table 1

u'_p	W'_{8m}	v'_{tmx}	$\frac{W'_{8m}}{v'_{tmx}}$	W'_{8m}	v'_{tmx}	$\frac{W'_{8m}}{v'_{tmx}}$	W'_{8m}	v'_{tmx}	$\frac{W'_{8m}}{v'_{tmx}}$	W'_{8m}	v'_{tmx}	$\frac{W'_{8m}}{v'_{tmx}}$
0.50										.101	.681	.148
0.55										.222	.779	.285
0.60										.349	.826	.422
0.65							.062	.242	.257	.469	.859	.547
0.70							.144	.479	.301	.578	.884	.654
0.75							.236	.588	.402	.675	.906	.745
0.80				.117	.153	.768	*.329	.654	.502	.761	.927	.821
0.85				.192	.324	.592	.417	.702	.594	.836	.946	.883
0.90				.269	.428	.627	.500	.741	.674	.901	.966	.934
0.95	.212	.155	1.37	.344	.503	.685	.576	.775	.743	.959	.985	.974
1.00	.280	.269	1.04	.417	.562	.743	&.646	.806	.802			
1.05	.346	.357	.971	.486	.612	.795	.710	.835	.851			
1.10	.411	.428	.959	.551	.656	.840	.769	.863	.891			
1.15	.473	.491	.965	.613	.697	.879	.823	.891	.924			
1.20	.533	.546	.975	.670	.736	.910	.873	.918	.951			
1.25	.590	.598	.986	.724	.774	.936	.920	.946	.972			
1.30	.643	.647	.995	.775	.811	.956	.963	.974	.988			
1.35	.695	.693	1002	.823	.847	.972						
1.40	.743	.738	1008	.868	.883	.983						
1.45	.790	.782	1011	.910	.918	.991						
1.50	.834	.824	1012	.951	.954	.997						
1.55	.876	.866	1011	.989	.990	1.00						
1.60	.916	.908	1009									
1.65	.955	.949	1006									
1.70	.991	.990	1001									
	v'_{tpx} = 0.60			= 0.70			= 0.80			= 0.90		

If we position the new probe particles at $x_p = x_o \pm u_{px}\tau_x$, we have

$$W_{8o}\left(v_{tox}^2\tau_x^2\right) = W_{8m}\left[v_{tmx}^2\tau_x^2\right] + 2W_{8p}\left[v_{tpx}^2\tau_x^2 + u_{px}^2\tau_x^2\right],$$

showing that the second spatial moment is also preserved by the velocity fragmentation.

2.3. Transformation from velocity-shear to spatial-shear

The ability of the distribution internal to a CPK particle to evolve in time, consistent with collisionless expansion, has been achieved by adding additional terms into the internal degrees of freedom of the basis particle. This distribution Eq. (2.1.2) is termed a "τ" particle form because the space part of the Gaussian has an additional contribution to its location from the product of internal time τ and velocity. As we have just shown, this form can be fragmented into additional particles that will be used to probe for new features, primarily in velocity space. It is also apparent that, perhaps with less physical justification, another particle form could be constructed in which the additional term goes into the velocity part of the Gaussian. We now show that a distribution of *exactly the same content* can be constructed with the form

$$f(\vec{x},\vec{v}) = \frac{W_{8o}}{(2\pi)^3 W_{dox}V_{tox}W_{doy}V_{toy}W_{doz}V_{toz}} \exp\left\{ -\left[\frac{\left(\vec{x}-\vec{x}_o\right)^2}{2\vec{W}_{do}^2} + \frac{\left[\vec{v}-\vec{u}_d-\vec{R}_p\left(\vec{x}-\vec{x}_o\right)\right]^2}{2\vec{V}_{to}^2} \right] \right\}, \tag{2.3.1}$$

where the capital $\vec{W}_{do}, \vec{V}_{to}$ are the new half-widths and where term $\vec{R}_p(\vec{x}-\vec{x}_o)$ uses the same vector notation as (2.1.2a). The combination $\vec{u}_d + \vec{R}_p(\vec{x}-\vec{x}_o)$ makes the effective average drift of the real particles that

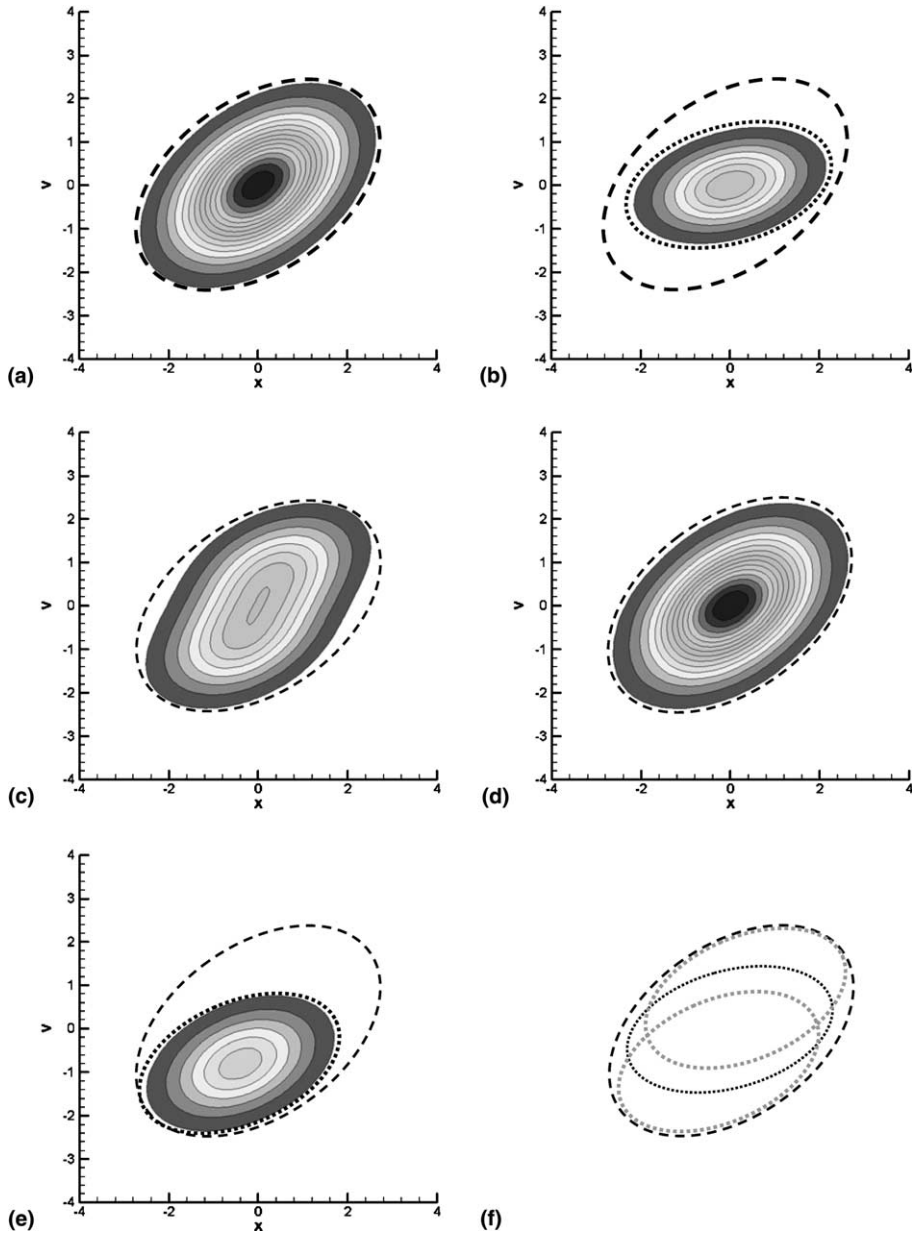

Fig. 2. An example of velocity fragmentation of the basic CPK particle using the * parameters from Table 1 that give nearly equal mass fragments with differing temperatures. Shown in (a) is the time-evolved particle in Fig. 1(b). Shown in (b) is the middle particle associated with the velocity fragmentation of (a). In (c) are the two probe particles showing the displacement in velocity. Shown in (d) is the sum of the middle particle (b) and the two probe particles (c). Ideally (d) is the same as the original (a); actually, the $L2$-norm of the difference between (a) and (d) divided by the $L2$-norm of (a) alone is less than 0.005. Shown in (e) is the lower probe particle by itself to accentuate the differences between the middle and each probe particle. In (f) are the outlines of the ellipses made from the half-widths in space and velocity for the three new particles. Note that in this case, all particles are cooler, thus appearing to have greater velocity-shear than the original.

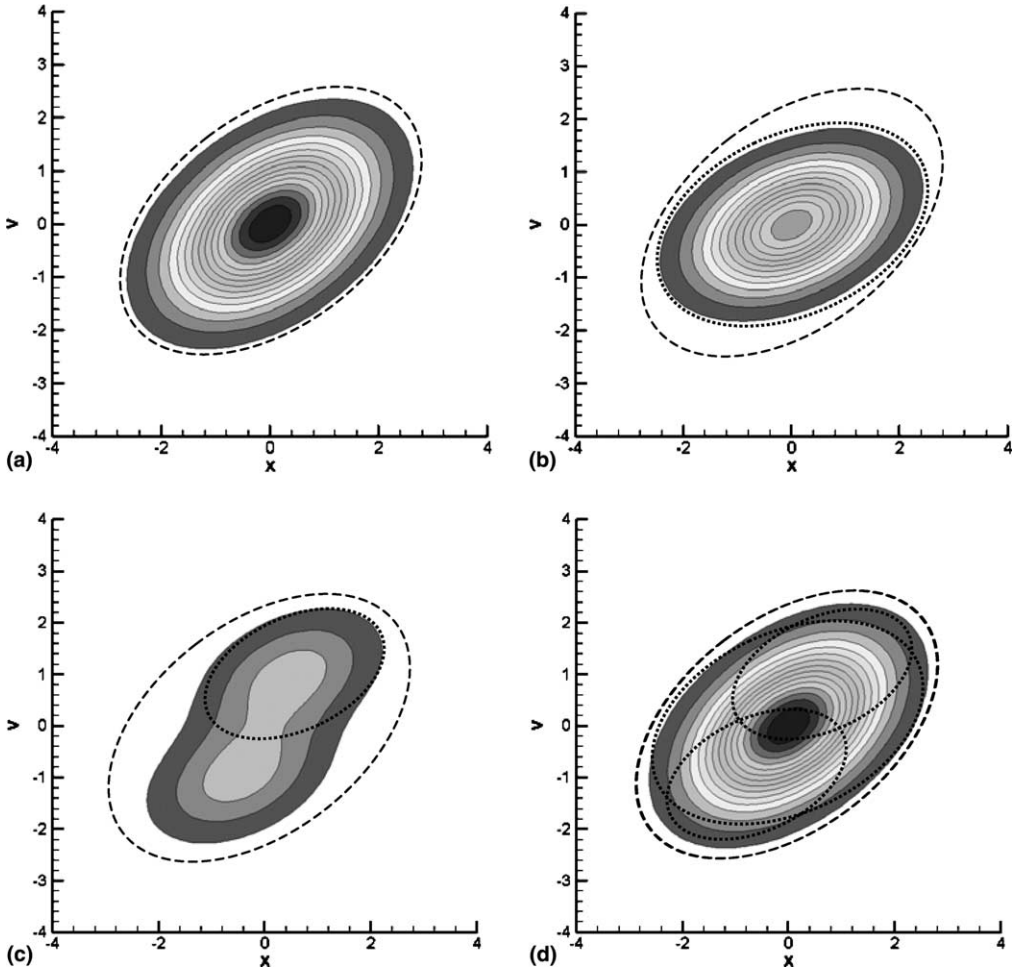

Fig. 3. Another example of velocity fragmentation of the basis CPK particle, this time using the & parameters from Table 1 which feature fragments with nearly equal temperatures. As before, we start with the original particle (a)—the same as in Fig. 1(b). Shown in (b) is the middle particle associated with the velocity fragmentation of (a). In (c) are the two probe particles showing a displacement in velocity. Shown in (d) is the sum of (b) and (c). The $L2$-norm has comparable accuracy to that in Fig. 2. Again, note that fragmentation makes cooler particles with increased W_{dx}/v_{tx}.

make up this macro CPK particle spatially dependent. $\vec{R}_p(\vec{x}-\vec{x}_o)$ is a measure of this "internal" mean drift relative to the drift of the center of the particle where $\vec{R}_p$ is the spatial shear term

$$\vec{R}_p \equiv \frac{\Delta\vec{v}}{\Delta\vec{x}}.$$

To construct $\vec{R}_p$ that preserves the contents of the distribution, the arguments of the exponentials in "$\vec{\tau}$ space" are equated with those in "$\vec{R}_p$ space". Thus,

$$\frac{(x-x_o)^2}{2W_{dox}^2}+\frac{\left[v_x-u_{dx}-R_p(x-x_o)\right]^2}{2V_{tox}^2}+y,zterms=\frac{\left[x-x_o-(v_x-u_{dx})\tau_x\right]^2}{2w_{dox}^2}+\frac{(v_x-u_{dx})^2}{2v_{tox}^2}+y,zterms. \tag{2.3.2}$$

Defining $\vec{\delta} \equiv \vec{x} - \vec{x}_o$ and $\vec{\delta}_v \equiv \vec{v} - \vec{u}_d$ and simplifying, we can solve for the components of $\vec{V}_{to}$, $\vec{W}_{do}$, and $\vec{R}_p$ which are the unknown parameters of the new space-sheared R-particle. Using the x component as the example, equating like powers of the independent variables, $\delta_{v_x}^2$, δ_{v_x}, δ_x, and δ_x^2 gives

$$\delta_{v_x}^2: \qquad \frac{1}{V_{tox}^2} = \frac{\tau_x^2}{w_{dox}^2} + \frac{1}{v_{tox}^2},$$

$$\delta_{v_x}\delta_x: \qquad \frac{-2R_{px}}{2V_{tox}^2} = \frac{-2\tau_x}{2w_{dox}^2},$$

$$\delta_x^2: \qquad \frac{1}{2W_{dox}^2} + \frac{R_{px}^2}{2V_{tox}^2} = \frac{1}{2w_{dox}^2},$$

respectively. Simplifying, these equations become

$$V_{tox}^2 = \frac{w_{dox}^2 v_{tox}^2}{w_{dox}^2 + v_{tox}^2\tau_x^2} = \frac{w_{dox}^2 v_{tox}^2}{W_{dox}^2}, \tag{2.3.3}$$

$$R_{px} = \frac{V_{tox}^2\tau_x}{w_{dox}^2} = \frac{v_{tox}^2\tau_x}{w_{dox}^2 + v_{tox}^2\tau_x^2}, \tag{2.3.4}$$

and

$$W_{dox}^2 = \frac{w_{dox}^2 V_{tox}^2}{V_{tox}^2 - R_{px}^2 w_{dox}^2} = w_{dox}^2 + v_{tox}^2\tau_x^2. \tag{2.3.5}$$

We can also find an expression for $\dot{W}_{dox}$. Differentiating with respect to time, we have

$$2W_{dox}\dot{W}_{dox} = 2v_{tox}^2\tau_x \rightarrow \dot{W}_{dox} = v_{tox}^2\tau_x/W_{dox}$$

which, combining (2.3.4) and (2.3.5), gives

$$\dot{W}_{dox} = R_{px}W_{dox}. \tag{2.3.6}$$

It is apparent that the R-space representation of the particle width W_{dox} evolves in accord with (2.3.6) even though the τ-space representation w_{dox} is independent of time.

It is easy to see that the new space-sheared particle has V_{tox} slightly colder and W_{dox} slightly bigger than the equivalent $\tau > 0$ velocity-sheared particle. Substituting (2.3.5) into (2.3.3) gives

$$W_{dox}^2 V_{tox}^2 = w_{dox}^2 v_{tox}^2$$

so that the normalization is preserved. It is interesting to note in (2.3.4) that $R_{px} = 0$ for both $\tau_x = 0$ and $\tau_x = \infty$. Differentiating R_{px} with respect to τ_x shows that the maximum occurs when $R_{px}\tau_x = 1/2$. At this point $\tau_{xR\max} = w_{dox}/v_{tox}$ giving $R_{px\max} = v_{tox}/2w_{dox}$.

Finally, it is just as easy to go from a space-sheared particle back to a velocity-sheared particle by reversing this process. The equations are

$$v_{tox}^2 = V_{tox}^2 + R_{px}^2 W_{dox}^2, \tag{2.3.3a}$$

$$\tau_x = \frac{R_{px}W_{dox}^2}{V_{tox}^2 + R_{px}^2 W_{dox}^2}, \tag{2.3.4a}$$

and

$$w_{dox}^2 = \frac{W_{dox}^2 V_{tox}^2}{V_{tox}^2 + R_{px}^2 W_{dox}^2}. \tag{2.3.5a}$$

The ability to transform from velocity-shear τ particle to space-shear R particle greatly facilitates many of the operations that will be required to take full advantage of the CPK representation. For example, velocity moments such as number density $n(\vec{x})$ require integration over all velocity. Velocity integration of the velocity-sheared distribution (2.1.2) is encumbered by the mixture of position and velocity in the position argument of the exponential. The equivalent space-shear distribution in (2.3.1) is easy to integrate—a shift in the location of the velocity peak of the Gaussian is irrelevant to the value of the integral. Additionally, as in Section 2.2 where we discussed how to fragment a τ particle in velocity space, we will next show how a velocity-sheared R particle can be similarly fragmented in position space.

2.4. Fragmentation in space

In Section 2.2, the velocity fragmentation of a velocity-sheared CPK particle was developed and the fragments were shown to nearly reproduce the original particle. In Section 2.3, it was shown that the distribution from a velocity-sheared particle could equivalently be obtained from a particle with a spatially dependent shear in velocity. The two identical distributions

$$f(x,v) = \frac{W_{8o}}{(2\pi)^{3/2} w_{dox} v_{tox} w_{doy} v_{toy} w_{doz} v_{toz}} \exp\left\{ -\left[\frac{\left[\vec{x} - \vec{x}_o - \left(\vec{v} - \vec{u}_d\right)\vec{\tau}\right]^2}{2\vec{w}_{do}^2} + \frac{\left(\vec{v} - \vec{u}_d\right)^2}{2\vec{v}_{to}^2} \right] \right\}$$

(velocity-sheared),

$$f(x,v) = \frac{W_{8o}}{(2\pi)^{3/2} W_{dox} V_{tox} W_{doy} V_{toy} W_{doz} V_{toz}} \exp\left\{ -\left[\frac{\left(\vec{x} - \vec{x}_o\right)^2}{2\vec{W}_{do}^2} + \frac{\left[\vec{v} - \vec{u}_d - \vec{R}_p\left(\vec{x} - \vec{x}_o\right)\right]^2}{2\vec{V}_{to}^2} \right] \right\}$$

(space-sheared)

suggest, by symmetry, that a procedure analogous to the one developed to do velocity fragmentation of velocity-sheared particles can be used for space fragmentation of a space-sheared particle.

To fragment a CPK particle in space, a velocity-sheared particle is first transformed to a space-sheared particle and then fragmented in space. Given x'_p (displacement from the center of the original particle as a multiple of W_{dox}) and W'_{dpx} (probe spatial width as a multiple of W_{dox}), we form

$$\alpha \equiv x'_p / W'_{dpx},$$

$$\beta_1 \equiv 2W'_{dpx} \exp\left(-\alpha^2/2\right) + \sqrt{2\pi} x'_p \operatorname{erf}(\alpha/\sqrt{2}),$$

$$\beta_e \equiv 2W'^2_{dpx}\left[1 + \alpha^2\right]$$

and then solve

$$W'_{8p} = (2\beta_1 - 2 - \beta_e)/(\beta_1^2 - 2\beta_e), \tag{2.4.1}$$

$$W'_{8m} = 1 - 2W'_{8p}, \tag{2.4.2}$$

$$w'_{dmx} = (1 - W'_{8p}\beta_1)/W'_{8m} \tag{2.4.3}$$

and set

$$u_p = R_p W_d. \tag{2.4.4}$$

Comparing this space fragmentation procedure with the previous velocity procedure, we here use x'_p in place of u'_{dx} and W'_{dpx} in place of v'_{tx} in the expressions for α, β_1 and β_e.

Finally, Table 1 guides the choice of x'_p and W'_{dpx} that lead to reasonable values for W'_{8m}, W'_{8p}, and W'_{dmx}. The thermal velocities of all three fragments remain the same as the original. An example of spatial fragmentation, using the & case from Table 1, is shown in Figs. 4 and 5.

2.4.1. 3-D Considerations

Section 2 to this point has been concerned with fragmentation of CPK particles in 1-D. When either a velocity or a spatial fragmentation occurs, parameters change in only that vector component. As shown in the spatial fragmentation shown schematically in Fig. 6, the other two directions remain unchanged. Thus, for each particle we must store $\vec{x}$, $\vec{W}_d$, $\vec{u}_d$, $\vec{V}_t$, and $\vec{R}_p$ or $\vec{\tau}$ vectors. If we choose to do, for example, a spatial split using the same splitting parameters in each direction, we can preserve the velocity anisotropy of the original particle in each of the fragments. We may choose however to fragment particles only in a single direction at a given time perhaps predicated on the resolution needs in that direction or to reduce growing anisotropy/particle elongation.

Finally, we note that it is possible to combine both the position and velocity fragmentation into a single operation. Shown in Fig. 7 are the original particle in (a), its nine constituents in (b), followed by the superposition of these nine distributions shown in (c). The superposition is very similar to the original; the peak of the reassembled particle (c) is roughly a percent higher than the original.

2.5. Merging

The goal of the merging process in CPK particles is fundamentally different than that of the fragmentation process. With fragmentation, the intent is to add computational resolution while preserving existing features. With the increased resolution resulting from fragmentation of particles, the resulting smaller particles have slightly different velocities or positions and can be expected to respond differently than their nearby neighbors in phase space thus retaining more of the richness inherent in the kinetic description. Considerable care has been used to insure that new, non-physical detail is not added in this process. In strong contrast, merging particles takes place only when, by some standard, the physics activity no longer warrants such high resolution. Merging of particles then takes place in those regions in which the physics content of a large number of particles could, without loss of salient features, be represented by fewer particles. Some microscopic details of the representation will be lost. The only benefit of merging is economy but, given the aggressive nature of fragmentation, this benefit is compelling.

There are two parts to the merging procedure that we now use: First, we decide which particles are "close enough" in phase space to be merged without excessive loss of macroscopic detail. Second, all merging

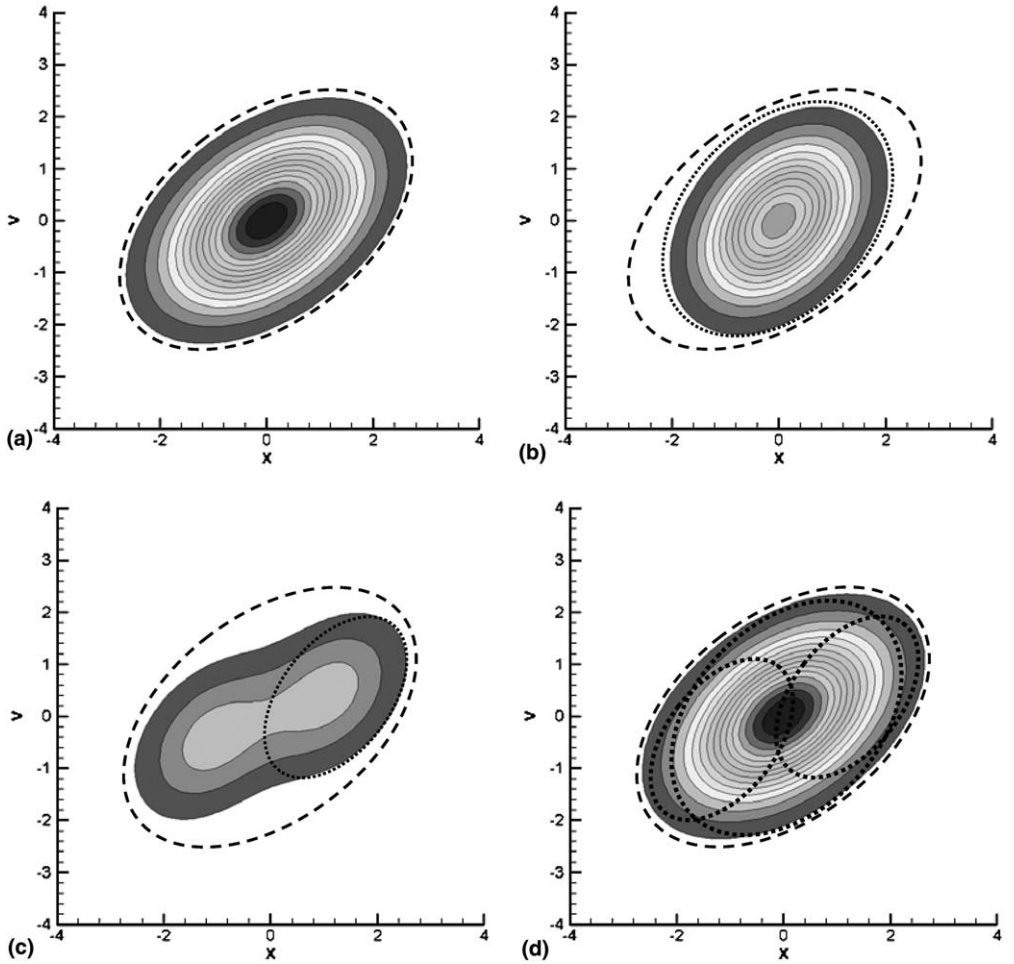

Fig. 4. An example of spatial fragmentation of a CPK particle. Shown in (a) is the R particle that is identical to the τ particle in Fig. 3(a). The new middle particle (b) now has a reduced W_d that corresponds to the velocity cooling of the middle particle in Fig. 3(b). The two probe particles (c) show the obvious displacement in space. Shown in (d) is the sum of the three particles, again nearly identical with the original (a). Note that space fragmentation makes particles relatively hotter and smaller; their W_d/v_t has decreased, the opposite of velocity fragmentation.

schemes ultimately come down to merging two CPK particles into one; we must build the internal parameters of this single particle to best represent the parameters of its constituents.

How can we join to two CPK particles into a single particle?

Once a particle has been deemed "close enough" to the emerging average particle to be joined with it, we need to specify just how these two particles can be joined. As we join nearby pairs, one particle lp disappears into the other particle av, which grows. Starting in R space, we first conserve

$$\text{Mass:} \quad W_{8cm} = W_{8lp} + W_{8av}, \tag{2.5.1}$$

$$\text{Momentum:} \quad \vec{u}_{dcm} = \frac{W_{8lp}\vec{u}_{dlp} + W_{8av}\vec{u}_{dav}}{W_{8cm}}, \tag{2.5.2}$$

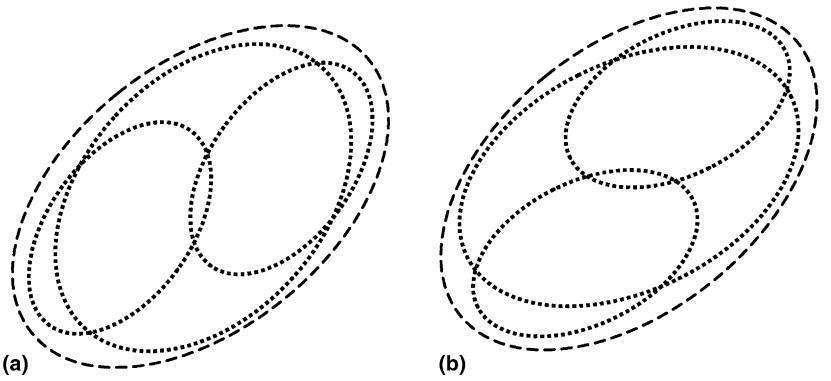

Fig. 5. In (a) are the envelopes of the three particles that result from spatial fragmentation shown in Fig. 4. For comparison, (b) shows the envelopes of the three particles that result from velocity fragmentation, shown in Fig. 3.

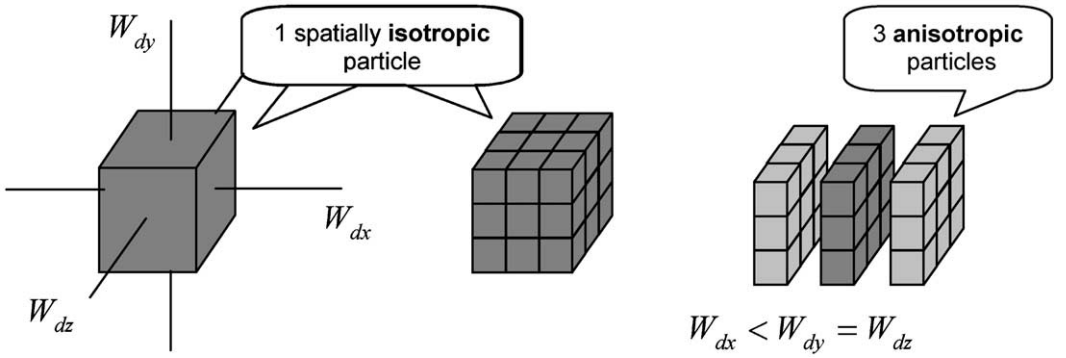

Fig. 6. A schematic presentation of a spatial fragmentation of the basic CPK particle. Shown on the left is a representation of a particle that is isotropic in $\overline{W}_d$. In the middle is the same particle with scribe marks showing the 27 isotropic particles that would result from fragmentation in all three directions. On the right are shown the three anisotropic particles that result from a single spatial fragmentation in the x direction.

$$\vec{X} \text{ moment}: \qquad \vec{x}_{cm} = \frac{W_{8lp}\vec{x}_{lp} + W_{8av}\vec{x}_{av}}{W_{8cm}}, \tag{2.5.3}$$

where the subscript cm denotes center of mass. Next we conserve the second spatial moment in each direction. Starting with $\langle x^2 \rangle$, we have

$$\begin{aligned} W_{8cm}W_{dcmx}^2 &= W_{8lp}[W_{dlpx}^2 + (x_{lp} - x_{cm})^2] + W_{8av}[W_{davx}^2 + (x_{av} - x_{cm})^2], \\ W_{dcmx}^2 &= \frac{[W_{dlpx}^2 + (x_{lp} - x_{cm})^2] + W_{8av}[W_{davx}^2 + (x_{av} - x_{cm})^2]}{W_{8cm}} \end{aligned} \tag{2.5.4}$$

with corresponding expressions for W_{dcmy} and W_{dcmz} . Now we conserve energy in each direction, using x for this example,

$$\begin{aligned} W_{8cm}\left(V_{tcmx}^2 + u_{dcmx}^2 + R_{pcmx}^2 W_{dcmx}^2\right) &= W_{8cm}\left[\left(\alpha_{cmx}^2 + R_{pcmx}^2\right)W_{dcmx}^2 + u_{dcmx}^2\right] \\ &= W_{8lp}\left(V_{tlpx}^2 + u_{dlpx}^2 + R_{plpx}^2 W_{dlpx}^2\right) + W_{8av}\left(V_{tavx}^2 + u_{davx}^2 + R_{pavx}^2 W_{davx}^2\right), \end{aligned}$$

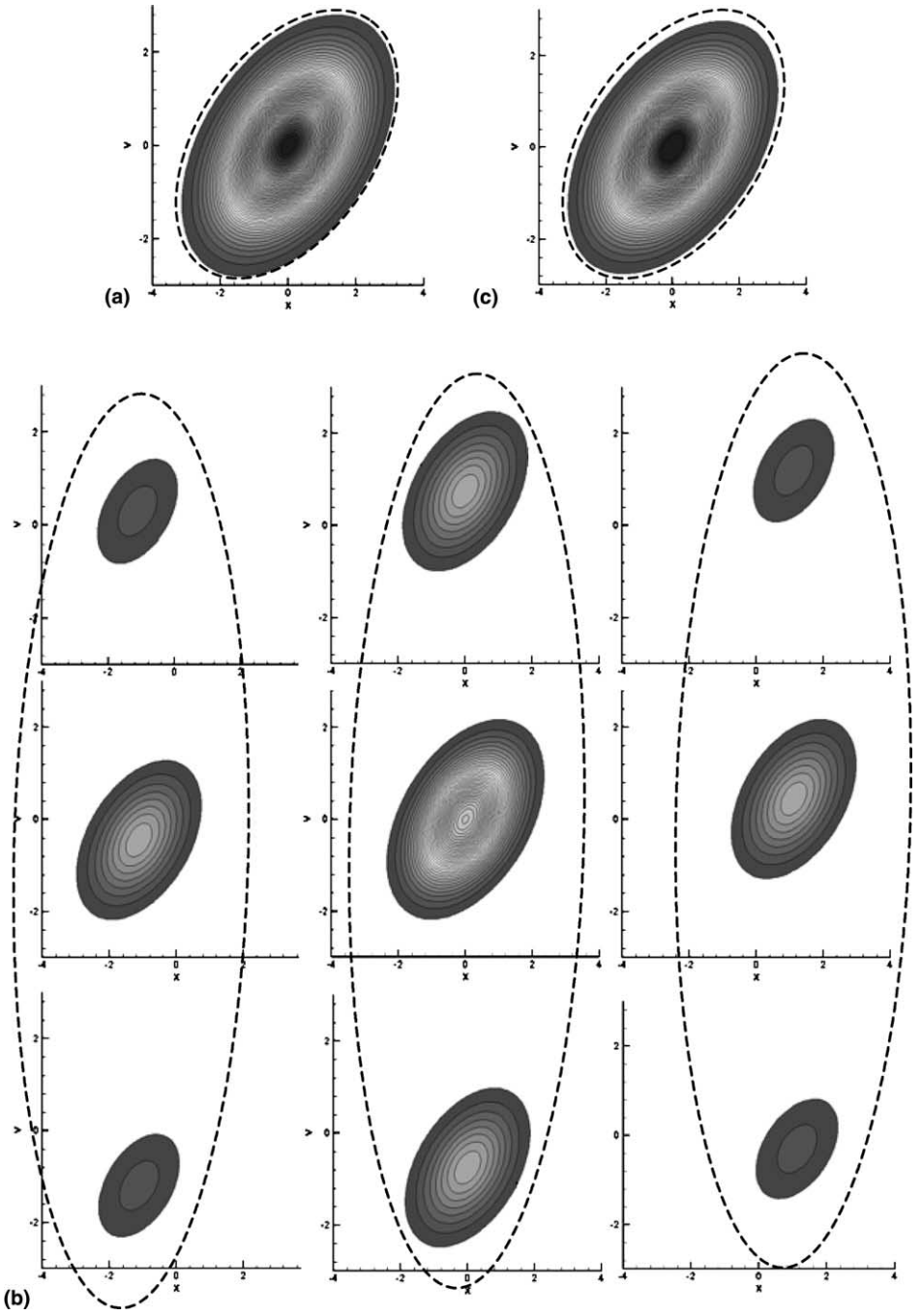

Fig. 7. (a) A particle that is fragmented, first in X then in V_X. (b) The result of that fragmentation with the dotted ellipses shown to schematically denote the initial X fragmentation. (c) The superposition of these nine particles that demonstrates the near recovery of the original particle. The reconstructed particle is slightly more peaked (by 1.04%) than the original.

where we have used $\vec{\alpha}_{cm} \equiv \vec{V}_{tcm}/\vec{W}_{dcm}$. Continuing, we find

$$\begin{aligned}(\alpha R)_x &\equiv \left(\alpha_{cmx}^2 + R_{pcmx}^2\right) \\ &= \left[W_{8lp}\left(V_{tlpx}^2 + \left(u_{dlpx} - u_{dcmx}\right)^2 + R_{plpx}^2 W_{dlpx}^2\right) + W_{8av}\left(V_{tavx}^2 + \left(u_{davx} - u_{dcmx}\right)^2\right.\right. \\ &\quad \left.\left. + R_{pavx}^2 W_{davx}^2\right)\right] \Big/ \left(W_{8cm} W_{dcmx}^2\right)\end{aligned} \tag{2.5.5}$$

with similar equations for y and z.

We find R_{pcmx} by evaluating the "weight" of each particle, $W_{8lp+} = W_{8lp}\mathrm{e}^{-(x-x_{lp})^2/2V_{txlp}^2}$ and $W_{8av+} = W_{8av}\mathrm{e}^{-(x-x_{av})^2/2V_{txav}^2}$, at the half-widths of the new center of mass particle $x_{cm\pm} = x_{cm} \pm W_{dxcm}$. We find a weighted drift velocity at these locations

$$U_{dxcm\pm} = \left[W_{8lp}R_{plpx}\left(x_{cm\pm} - x_{lp}\right) + W_{8av+}R_{pavx}\left(x_{cm\pm} - x_{av}\right)\right] \Big/ W_{8cm}$$

and use these to form the new velocity ramp term using

$$R_{pcmx} = \left(U_{dxcm+} - U_{dxcm-}\right)/2W_{dxcm}. \tag{2.5.6}$$

The other components are treated similarly.

We now have all the pieces needed to assemble a new V_{tcm} in each direction using

$$V_{tcmx}^2 = W_{dcmx}^2\left[(\alpha R)_x - R_{pcmx}^2\right] \tag{2.5.7}$$

with similar expressions for y and z. At the end of this procedure the center of mass particle becomes the new "average" particle.

Tests of this procedure, in Fig. 8, show its effectiveness as well as illuminate some of the issues associated with destroying details of the distribution contained in the unmerged set of particles. Consider first merging two identical particles, at the same spatial location but with drift velocities that differ slightly. Shown in (a) is the original particle *lp* and the second particle *av* is shown in (b). In panel (c) is the superposition of the distribution presented by these two particles and in (d) is the distribution carried in the single particle *cm* that results from this merging process.

Clearly the merging process does not preserve details of the distribution that might seem to be essential in "collisionless" physics. Even though the first three moments in both space and velocity are preserved and a "best" velocity ramp has been constructed, the distribution norm does grow in this process. In (c) the superposition of the two distributions, each with unit norm, has a height of 1.33—a result of adding the two particles. The new single particle (d) that represents these two originals has different shape because its must have a CPK particle format. The new particle has a norm of 1.48. This simple example makes obvious the fact that norm of the merged distribution will grow compared to purely collisionless behavior—a fact that will change the behavior of instabilities that depend on the slope of the distribution. Clearly, this growth must be considered when deciding which particles to merge.

A second, slightly more general example makes this trend even more obvious. In Fig. 9 are two particles with the same spatial location that differ in width, temperature, drift velocity, and velocity shear.

Before we discuss a procedure to select particles for merging, we consider a case in which particles should merge as a validation of the procedure. We show in Fig. 10 the results of a test that remerged the nine particles that resulted from the combined spatial and velocity particle split in Section 2.4.

Which particles should be joined?

The result of merging of any two particles can result in one new particle that is significantly different than the superposition of the two. If we are trying to preserve the distribution function, merging any two

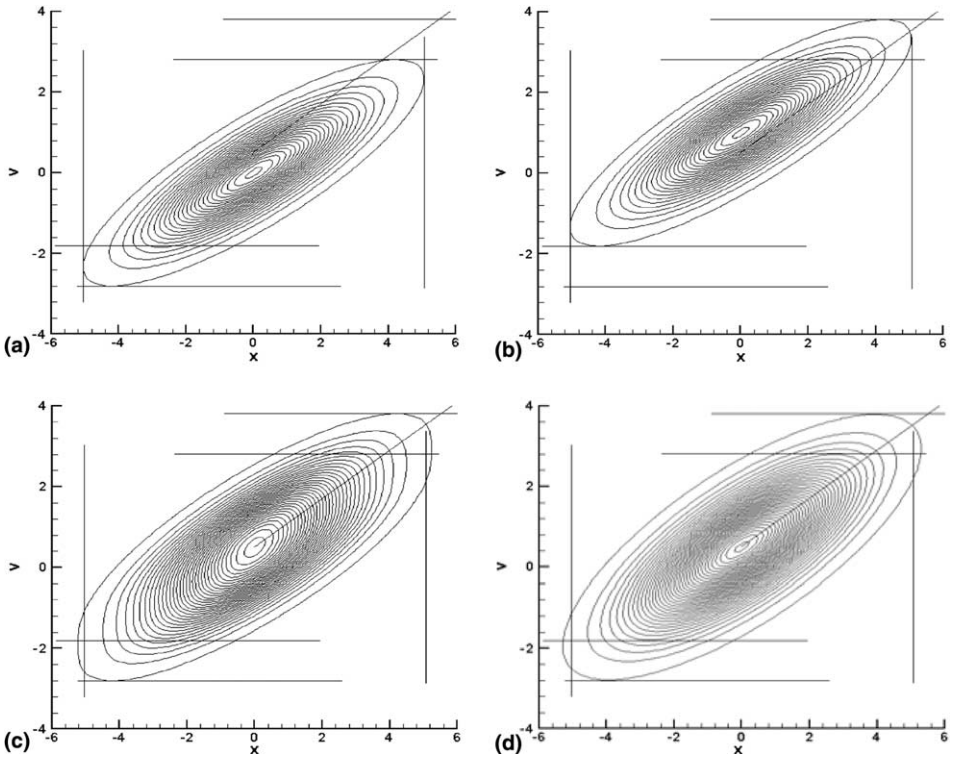

Fig. 8. (a) The original particle *lp* and the second particle *av* is shown in (b). In panel (c) is the superposition of the distribution presented by these two particles and in (d) is the distribution carried in the single particle *cm* that results from merging. The lines are added as a reminder of original particle dimensions and velocity ramps.

particles can be difficult to justify. It is often the case, however, that these subtleties are fully enveloped in the local average of nearby particles. In practice, it is often sufficient to compare individual particles with an average over all the particles properties within some region. We form a list of "average" particle quantities that includes, at least, the weight-averaged position, velocity, width, and thermal velocity. (In multi-dimensions, quantities such as angular momentum, etc. will be added to the list.) The concept is to form a composite particle, initially with zero weight, that has the other "average" particle parameters. We then compare each particle in the neighborhood (see Section 2.6) to the average and, if there is sufficient overlap between the two, merge this particle with the emerging composite particle. Thus the composite particle "becomes" the first actual particle with properties close enough to the average to be merged. Subsequent candidates for merging are selected by comparing to the original, average parameters. As the more particles are merged with the composite average, the composite particle grows in weight and its parameters move slightly to reflect the composite average of those particles it now represents. This merging process conserves mass, momentum, energy as the kinetic energy in the center-of-mass frame of the merging particles is added to the thermal energy in the growing, evolving composite particle.

Out of the multitude of possibilities for the merging, we start with this simple prescription. We define "overlap" in terms of three parameters: $effW_d$, $effV_t$, and $effR_p$. After defining the neighborhood particle averages, we require, taking spatial overlap as an example, that the lowest (greatest) "boundary" of a macro-particle, the location of the particle center minus (plus) W_{dx} be greater (less) than the center of the particle average minus (plus) $effW_d$ times the average W_{dx}. Thus we have exaggerated the size of the average by $effW_d$ and we require that the half-width of the particle to be merged be fully contained within this

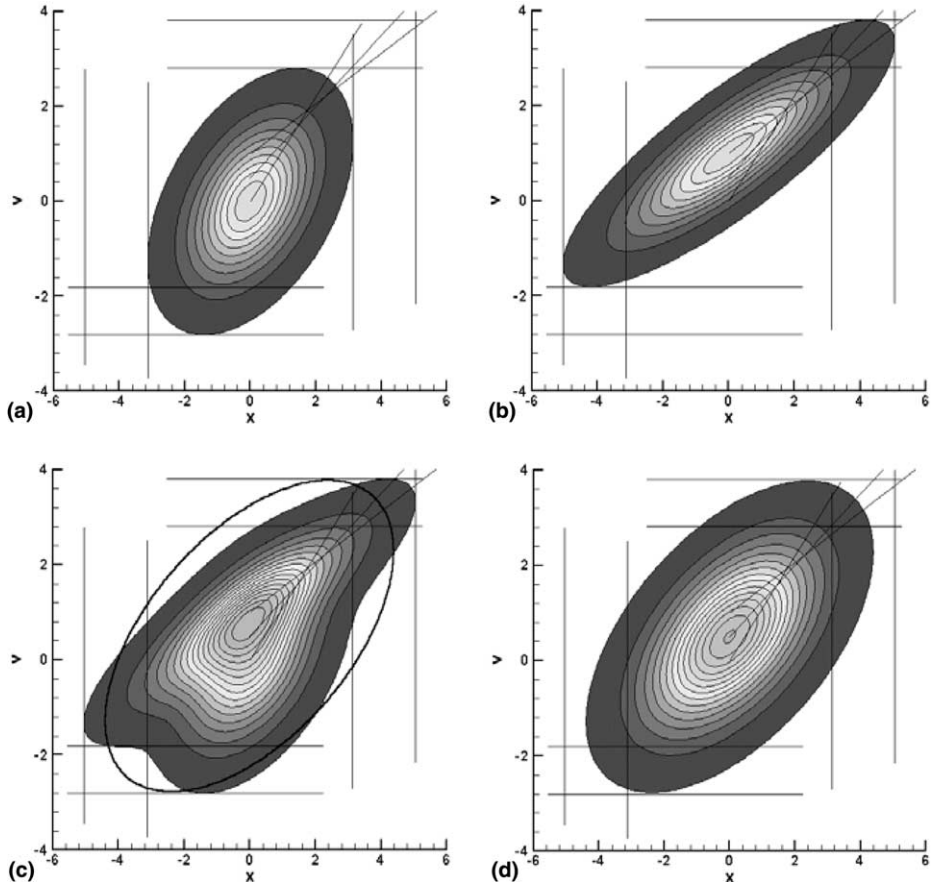

Fig. 9. As in Fig. 8, the original particle *lp* in (a), and the second particle *av* in (b) are superposed in (c). In (d) is the distribution carried in the single particle *cm* that results from merging. The oval in (c) is the last contour in (d). The lines are again added as a reminder of original particle dimensions and velocity ramps.

enlarged average. Due to the symmetry between x and v, exactly the same procedure can be used in velocity space, using $effV_t$ in place of $effW_d$.

This is a rather crude merging concept. However, the procedure works well enough, in practice, to serve as springboard to more effective concepts. For example, we are now reconsidering how to employ overlap integrals that can be done analytically. However, such integrals would require particle–particle evaluations, leading to N^2 interactions, at least locally, compared to the $2N$ interactions in this procedure that builds an average (N) and then compares particles to that average (the second N).

For the results shown in this paper, we will use only the original overlap concepts. In addition, we have subdivided the neighborhood in to smaller bins, each bin having width $\delta v_{tavg}\Delta t/2$. These bins are functionally equivalent to the full neighborhood described above. The tolerances-for-merging parameters, $effW_d$, $effV_t$, and $effR_p$, are now required input for the algorithm. Fortunately, these parameters affect the physics only indirectly through the smoothing that comes from averaging hopefully insignificant details. Further details of the present implementation will be given following the section describing the particle data structure.

Ultimately, merging may be desirable in distributions that are more complex. For example, interpenetrating flows clearly have multi-peaked distributions with few particles overlapping with an average particle

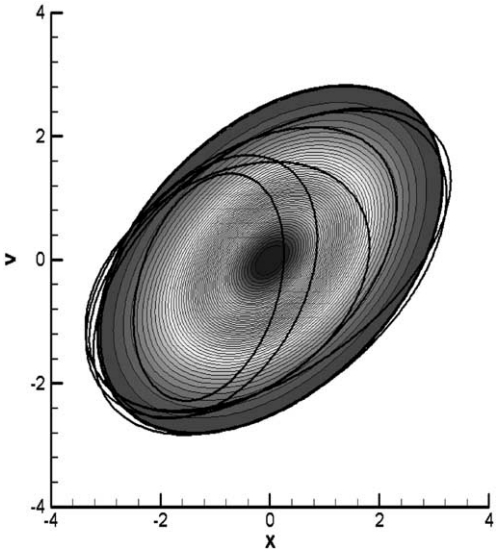

Fig. 10. Shown here are the outside contours that result from the merging of the particles from the fragmentation in Fig. 7. The smallest contour is the result of merging only the upper and lower left. The next larger contour is the result of adding the middle particle on the left to the "average" particle that resulted from first merging. In the next larger contour, the middle particle on the right was merged to the average, followed by the upper then lower right. The sequence was completed by merging the lower, middle, and upper particles in the middle column of Fig. 7, respectively. The final "average" particle is very similar to the original; the peak of the final average was 1.0102 compared to 1.0000 for the original.

with global average velocity. It is feasible in such cases to define more than one "average" particle each initiated at the point in phase space that has the feature to be retained. Details of this algorithmic extension have yet to be worked out.

2.6. Data management: stringers versus mesh points

The process just described is of order $2N$ operations where N is the number of macro-particles in the vicinity. We define this number as that number of particles contained in a linked list of particles whose center is closer to this "stringer" point than any other. Thus, much like a traditional grid point, there is a volume of space centered about these stringer points. To process all particles in that can locally affect the physics at a stringer point, we start with the first particle in the list and proceed until the list is complete.

For diagnostics, these stringer points are good locations to accumulate densities, etc. When we use this method for plasma simulations, we suspect that these stringer locations with also be good locations to compute electromagnetic fields from these densities. Thus for plasma simulation, the distinction between "stringer points" and "mesh points" is minimal. The distinction is retained however to emphasis that the stringer "mesh" is *almost* irrelevant to the transport part of the algorithm. Recall that all transport is accomplished by expansion of individual particles and subsequent fragmentation of these growing particles. Since *no gradient of pressure is ever explicitly computed*, the array of stringers simply amounts to a choice in data organization. We can redefine the stringer locations at any time to a more advantageous set and then reassign the particles to lists consistent with these new locations. The location of stringers does have a small effect in the merging operation because particles near the boundary between two stringers are less likely to overlap with the stringer average. For systems that are far from collision-dominated, the effect becomes negligible. It is straightforward to consider combinations of stringers to mitigate such problems but, obviously, this is an area of ongoing research.

An integral part of the present algorithm is a straightforward procedure to move the macro-particles to the appropriate stringer as they move in space. Thus each particle remains sorted in space as the particle ensemble moves forward in time. For the present 1-D embodiment, we are using uniformly spaced stringers but the generality to add a stringer at any arbitrary point at our convenience is available and expected to aid in the adaptability of multi-dimensional versions. (We suspect this feature will be useful in MPP versions in which domain balancing could easily be accomplished by moving stringers located near a domain boundary to the adjacent domain.)

2.7. Time integration cycle

The point of developing these procedures for handling particles is to allow or facilitate an adaptive resolution particle-based code to "probe for emerging features". With the emphasis on preserving the distribution functions within the particles and preserving the composite distribution of the ensemble, we now consider the time integration algorithm that allows the "probing" to occur. The fundamental concept is to generate the greatest number of particles, thus the best resolution in phase-space parameters, just before the particles are exposed to the nonlinear forces that modify their velocities. An example from plasma physics is that many instabilities occur when particles with just the right position and velocity resonate with electromagnetic waves. The more particles in the representation, the greater the number that will resonate with this wave and allow the "feature" to grow out of the noise. The coarser the resolution, the more likely it is that coherent growth of the feature will be disrupted by noise.

To optimally probe for new features, we want to have the greatest resolution just before the particles move. There are two operations that change the particle's phase-space coordinates: (1) the traditional Lagrangian position and velocity advance and (2) the increment to the internal time τ. Incrementing the internal time is the step that allows the particle to expand due to internal dynamics and this expansion, after fragmentation, results in probe particles at positions and velocities that differ from the original particle. For (1), we desire the best spatial and velocity resolution just before the Lorentz force velocity update where small differences in position and velocity can make a critical difference in the forces exerted on the particle. These differences in the forces felt by nearby particles are reflected in the new velocities and, later, the positions of the nearby particles. It is these differences that allow the capture emerging features in phase space.

When the internal time of a particle is incremented (2), it is evident, from Fig. 1, that the center of the particle does not move. However, the spatial extent of the particle has expanded consistent with the particle's internal evolution. When this "older" particle is fragmented, both probe particles have positions and velocities that deviate from the original particle, constituting mass movement in phase space. It may be that this motion, due to purely internal influences, is inconsistent with the mass motion slowed by external influences. For example, the internal free expansion, affected by $\tau = \tau + \Delta t$, can be larger than would be tolerated by charged particle motion across a magnetic field. To avoid such inconsistencies, we first do the fragmentation then the Lagrangian advance. Key aspects of this problem are detailed in Fig. 11.

The need to fragment particles, perhaps both in space and in velocity, the need to transform from τ to R and back, and the need to merge, all in addition to the traditional particle Lorentz force advance and electromagnetic field solution, allows a large number of possibilities for the sequence of operations. It is probable that CPK will have its own preferences and will make these known as we expand the envelope of test cases. With this caveat, we present the sequence of operations now used.

Assume that the particle locations and internal properties have all been initialized at time level $t = n * \Delta t$ and various electromagnetic fields and source quantities are available on a spatial mesh. The task is to advance the ith particle location and velocity x_n, v_n, the internal quantities w_{dn}, v_{tn}, τ_n (and $I\omega_n$

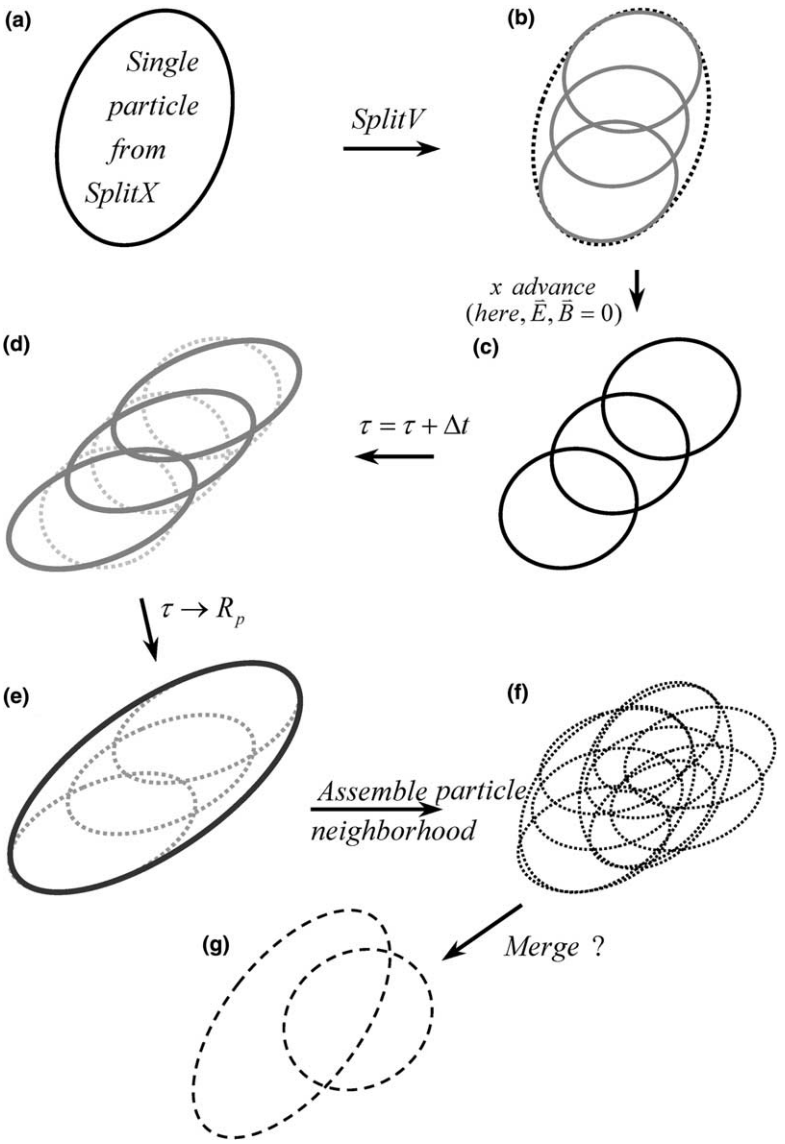

Fig. 11. Pictorial view of a CPK time step. In (a), we start with one of the particles that result from a space fragmentation. Moving to (b), a velocity fragmentation has been performed. In (c), the particles can be moved as a result of increments in position, followed, in (d), by a time increment on all the particles. Shown in (e) is the envelope of these three particles that is the same as would have been obtained (in this case with zero fields) by incrementing the internal time of the original particle. Pictorially in (f) we have shown the particles in the neighborhood that have been assembled for possible merging (g).

angular momentum, eventually) and e_n (internal energy) from time level n to $n+1$. At the start of this step, the fields $\vec{E}_{n+1/2}, \vec{B}_{n+1/2}$ and the source terms $\rho_{n-1/2}, \vec{J}_n$ are available. (This field algorithm is now in development and will be presented in a future publication.) Note that the position advance has been split into two half steps so that the position and velocity can be available at the same time level.

The present sequence is:

$\vec{x}_{in+1/2} = \vec{x}_{in} + \frac{\Delta t}{2} u_{din}$
TRAP (All particles) {*TRAP is the algorithm that processes particles that cross a domain or simulation boundary*}

V-SPLIT {*Velocity fragmentation*}
TRAP (New particles only)
$\vec{\tau}_{in+1/2} = \vec{\tau}_{in} + \Delta t/2$
Shift $\vec{\tau} \to \vec{R}_p$

$$\rho_{n+1/2} = \sum_i \frac{q_i W_{8i}}{2\pi \vec{W}_{di}} \int_{-\infty}^{\infty} d\vec{x} \exp\left(\frac{-(\vec{x} - \vec{x}_{in+1/2})^2}{\vec{W}_{di}^2}\right)$$

X-SPLIT (where necessary) {*Spatial fragmentation*}
Advance velocities {*Reflects contributions from external forces and self-consistent electromagnetic fields*}

$$u_{din+1} \Leftarrow u_{din} + \frac{q\Delta t}{m}\left[\vec{E}_{n+1/2}(\vec{x}_{in+1/2}) + \frac{u_{din+1} + u_{din}}{2c} \times \vec{B}_{n+1/2}(\vec{x}_{in+1/2})\right]$$

Shift $\vec{R}_p \to \vec{\tau}$
$\vec{x}_{in+1} = \vec{x}_{in+1/2} + \frac{\Delta t}{2} u_{din+1}$
TRAP (All)
$\vec{\tau}_{in+1} = \vec{\tau}_{in+1/2} + \Delta t/2$
Shift $\vec{\tau} \to \vec{R}_p$
MERGE
Velocity diagnostics and source accumulation at n+1

$$\vec{J}_{n+1} = \sum_i \frac{W_{8i}\vec{u}_{di}}{2\pi \vec{W}_{di}} \int_{-\infty}^{\infty} d\vec{x} \exp\left(\frac{-(\vec{x} - \vec{x}_{in+1})^2}{\vec{W}_{di}^2}\right)$$

COMPUTE FIELDS $\vec{E}_{n+3/2}, \vec{B}_{n+3/2}$ [Using $\rho_{n+1/2}, \vec{J}_{n+1}$]
Shift $\vec{R}_p \to \vec{\tau}$

2.8. Collision-dominated internal dynamics

In this algorithm in which each CPK particle is considered a full distribution of real particles in both velocity and space, two types of collisions must be considered. The most obvious is the collision between individual CPK particles. Such cases include individual CPK particles, representing a single species, interacting with a second species contained within a second macro-particle. For such interactions to occur, the macro-particles must be "near" one another in space and have a mutual cross-section that gives a finite probability for "collision". Such collisions will be used for ionization or other acts of "chemistry" in addition to the traditional elastic collisions and will be the subject of later publications. The other collision type is the internal collision. A distribution of particles within a CPK particle, shown in Fig. 1(a), will surely expand with time. Shown in Fig. 1(b) is, in fact, how the distribution evolves if individual real particles are allowed to simply free-stream—subject to no collisions within the macro-particle. In real particle distributions, collisions will occur within the macro-particle distribution.

To model such internal collisions, it is desirable for each CPK particle to have the ability to represent a collision-dominated expansion. To develop a collisional counterpart to the collisionless analytic within a CPK particle, the first step is to determine the particle's collisional evolution. Intuition can be misleading. Langevin's equation describes a collisional drag on individual particles towards the mean velocity in a few collision times, suggesting that the overall expansion of the macro particle distribution could be slowed by collisions. However, for the Gaussian spatial dependence of a CPK particle, a collisional system experiences a gradient in pressure that will drive particle expansion. Ultimately, we complemented our intuition with a hydrodynamics simulation of the evolution of a Gaussian-shaped particle with uniform initial temperature.

Simulation of a collision dominated, CPK-shaped fluid profile with a 1-D hydrodynamics code, Zimmerman, private communication [19], revealed that

(A) there are no shocks or rarefactions,
(B) the density retains a Gaussian shape,

$$n(\vec{x},t) = \frac{n_o}{(2\pi)^{3/2} W_{dx}(t)} \exp\left[-\frac{(x-x_o)^2}{2W_{dx}^2}\right]$$

(C) the internal velocity is linear in displacement from the particle center
$\vec{u}(\vec{x},t) = \vec{R}_p(t)(\vec{x}-\vec{x}_o)$
(D) the temperature $T(\vec{x},t)$, initially constant over the entire "particle", remains constant, a function only of time
$T(\vec{x},t) = T(t)$

In light of these observations, consider the 1-D hydrodynamics equations:

$$\text{Continuity}: \qquad \frac{\partial n}{\partial t} + u\frac{\partial n}{\partial x} + n\frac{\partial u}{\partial x} = 0, \tag{2.8.1}$$

$$\text{Momentum}: \qquad m\frac{\partial u}{\partial t} + mu\frac{\partial u}{\partial x} + \frac{1}{n}\frac{\partial P}{\partial x} = 0, \tag{2.8.2}$$

$$\text{Adiabatic EOS}: \qquad P = P(x,t=0)\left(\frac{n}{n(x,t=0)}\right)^{\gamma} = n(x,t)k_{\mathrm{B}}T(t). \tag{2.8.3}$$

Ignoring, for the moment, any gradients in y and z, we use observations A, B, C, and D as assumptions in Eqs. (2.8.1)–(2.8.3). The continuity equation (2.8.1) gives

$$n\frac{\dot{W}_d}{W_d}\left(\frac{(x-x_o)^2}{W_d^2} - 1\right) - nR_p\left(\frac{(x-x_o)^2}{W_d^2} - 1\right) = 0$$

or

$$\vec{R}_p = \frac{\vec{\dot{W}}_d}{\vec{W}_d} \tag{2.8.4}$$

when all components are considered. Note that this is the same as the collisionless expression (2.3.6). The momentum equation (2.8.2) gives

$$(x-x_o)\dot{R}_p + R_p(x-x_o)R_p + \frac{k_{\mathrm{B}}T}{nm}\frac{\partial n}{\partial x} = 0, \quad \dot{R}_p + R_p^2 - \frac{k_{\mathrm{B}}T}{mW_d^2} = 0 \tag{2.8.5}$$

and the adiabatic equation of state gives

$$T(t) = T(0)\left(\frac{W_{dx}W_{dy}W_{dz}}{W_{dx}(0)W_{dy}(0)W_{dz}(0)}\right)^{1-\gamma}, \tag{2.8.6}$$

where we have used $n = W_8/(W_{dx}W_{dy}W_{dz})$. If we differentiate (2.8.4), component by component, we get

$$\dot{R}_p = \frac{\ddot{W}_d}{W_d} - \frac{\dot{W}_d^2}{W_d^2} = \frac{\ddot{W}_d}{W_d} - R_p^2$$

and substitute into (2.8.5), we get

$$\ddot{\vec{W}}_d = \frac{k_B T}{m\vec{W}_d}. \tag{2.8.7}$$

Thus we see that the assumptions B, C, and D are consistent with the 1-D collision-dominated hydrodynamics equations when the width of the Gaussian W_d evolves as prescribed by Eq. (2.8.7) and the adiabatic relation (2.8.6) holds for T.

Now we consider the energy in this distribution. Multiplying (2.8.7) by $\dot{W}_d$, we get

$$\dot{W}_d\ddot{W}_d = \dot{W}_d\frac{k_B T}{mW_d} = k_B\frac{\dot{W}_d}{mW_d}T(0)\left(\frac{W_d}{W_d(0)}\right)^{1-\gamma},$$

$$\dot{W}_d\ddot{W}_d = \frac{k_B T(0)}{mW_d(0)^{1-\gamma}}\dot{W}_d W_d^{-\gamma},$$

$$\frac{\mathrm{d}}{\mathrm{d}t}\left(\frac{\dot{W}_d^2}{2}\right) = \frac{k_B T(0)}{mW_d(0)^{1-\gamma}}\frac{\mathrm{d}}{\mathrm{d}t}\left(\frac{W_d^{1-\gamma}}{(1-\gamma)}\right).$$

Integrating from $t = 0$ to t, using (2.8.6), we get

$$\left[\dot{W}_d^2(t) - \dot{W}_d^2(0)\right] = \frac{2k_B}{m(1-\gamma)}[T(t) - T(0)]$$

or

$$\begin{aligned} 2k_B T(t) + (\gamma-1)m\dot{W}_d^2(t) &= 2k_B T(0) + (\gamma-1)m\dot{W}_d^2(0)\frac{3}{2}k_B T(t) + (\gamma-1)\frac{3m}{4}\dot{W}_d^2(t) \\ &= \frac{3}{2}k_B T(0) + (\gamma-1)\frac{3m}{4}\dot{W}_d^2(0) \equiv E_R, \end{aligned} \tag{2.8.8}$$

which, for $\gamma = 5/3$ and using (2.8.4), gives the same expression obtained for the collisionless CPK particle (2.5.5). (Thus we can evolve this collision-dominated "particle" using (2.8.7) and either (2.8.6) or (2.8.8) to provide the temperature.)

The advantage of these profiles is that they have and retain the same form (Gaussian spatial profile, sheared Maxwellian velocity profile) as the collisionless CPK particle. Thus, all the fragmentation and merging capabilities previously developed for the collisionless particle evolution can be used for the collision-dominated, γ-law fluid evolution of a particle. Shown in Fig. 12 is the initial state (a) and the collisionless evolution in (b) of the collision-dominated evolution of a $\gamma = 5/3$ particle in (c). To follow this

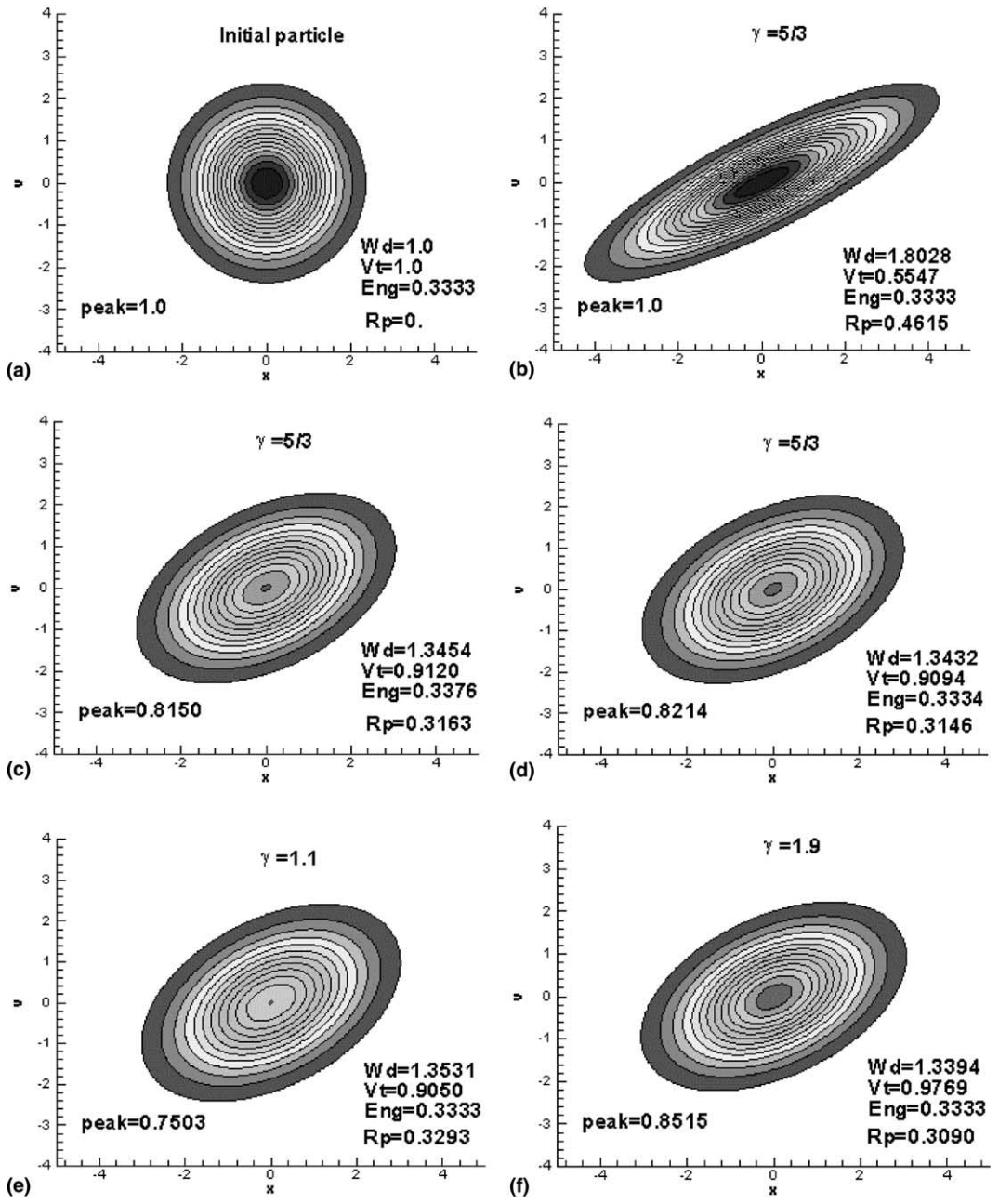

Fig. 12. A comparison of collisonless and collision-dominated CPK particle evolution. Starting from the particle in (a), collisionless evolution leads to the particles and associated parameters in (b) while the collision-dominated evolution leads to the particle and parameters shown in (c). In general, the collisional evolution is slower (W_d increases more slowly) and is slightly hotter ($V_{t\,\text{collisional}} > V_{t\,\text{collisionless}}$). In (d) is shown the same particle evolved with more, smaller time steps—demonstrating convergence. (e) and (f) show the same initial particle subjected to evolution with more extreme γs.

internal evolution of the particle, we have integrated (2.8.1) using a leap-frog scheme with an auxiliary variable $\dot{W}_d$ known at the half-time level of the integration.

3. Results

We present here the results obtained from our tests of the CPK algorithm, embodied in a code called KEYDRO. We performed tests in two limits: (A) collisionless and (B) collision dominated. The primary application of the CPK algorithm remains the partially collisional plasma physics regime and, to be useful, the partially collisional algorithm must, at least, work at both extremes. We expect that the ultimate partially collisional algorithm will be built with elements from these two models. We are currently investigating such possibilities that involve analytically computing the overlap of two particles in position space, computing collision cross-sections for the mutual fraction that overlaps given their relative drift and temperature, and forming new particles to collide from that fraction that is deemed to collide. We will likely employ Larson's extension [20] of an algorithm proposed by Miller and Combi [21] that reduces the number of parings required.

We judge the collisionless limit to be easier than the collision-dominated limit: our algorithm *is* a collisionless PIC model if we simply start with many, small macro-particles and inhibit both the fragmentation and merge procedures. For more ambitious examples, we present the first two extensions to pure PIC on a relatively simple collisionless free expansion of a gas into a vacuum. First, we run this expansion in a modified "PIC" limit in which we simply start with one CPK particle and let it fragment as it expands. The fragmentation eventually saturates as the individual particles become smaller in weight than an initially specified criteria. The "PIC" limit is recovered because no merging is allowed. Second, we compare this result with the case in which merging *is* allowed, thus demonstrating the essential step in economizing on the number of particles. Compared to the "PIC" limit that has many small, cold particles in its interior, the merging result shows the expected reduction of particles in the interior but retains small, cold particles in regions exterior to the core of the distribution, essential to capturing emerging features. These results are in Section 1.

In Section 2, we present the results of the first application of CPK in the fluid/collision-dominated limit. While the collision-dominated limit was not the intended application for CPK, the arbitrarily collisional applications require the algorithm to recover the collision-dominated limit, efficient or not. Our initial application, a shock tube problem [22], shows the algorithm to be more efficient than originally expected in this collision-dominated limit. More important for present purposes, the collisional limit is especially useful in demonstrating the capabilities and unusual features of fragmentation and merging.

3.1. Collisionless expansion of a gas puff into a vacuum

We initialize the $t = 0$ start of the collisionless expansion problem using one CPK particle with $\tau = 0$ in the center of a 1-D region $-10 \leqslant x \leqslant 10$ cm. This initialization is equivalent to beginning with a Gaussian gas puff with width w_{dx} containing W_{8t} real particles with a thermal velocity v_{tx}. For the case presented here these parameters have the values 0.25 cm, 10.0 real particles, and 1.0 cm/s, respectively. This particular run was made with 225 equally spaced stringer points and a time step of $\Delta t = 0.05$ s. We watch this expansion for $t = 3.0$ s. For comparison, the analytic solution is recovered by simply evaluating the original particle with the internal time parameter $\tau = 3.0$ s.

In Fig. 13 we see a configuration that results when both x and V_x fragmentation is allowed on every particle, every time step until the weight of the individual macro-particles become smaller than 0.0025 real particles. Shown in Table 2 is the evolution of the macro-particle number in the run. Below this minimum weight, no further fragmentation is allowed. We allow no merging in this run; individual particles simply

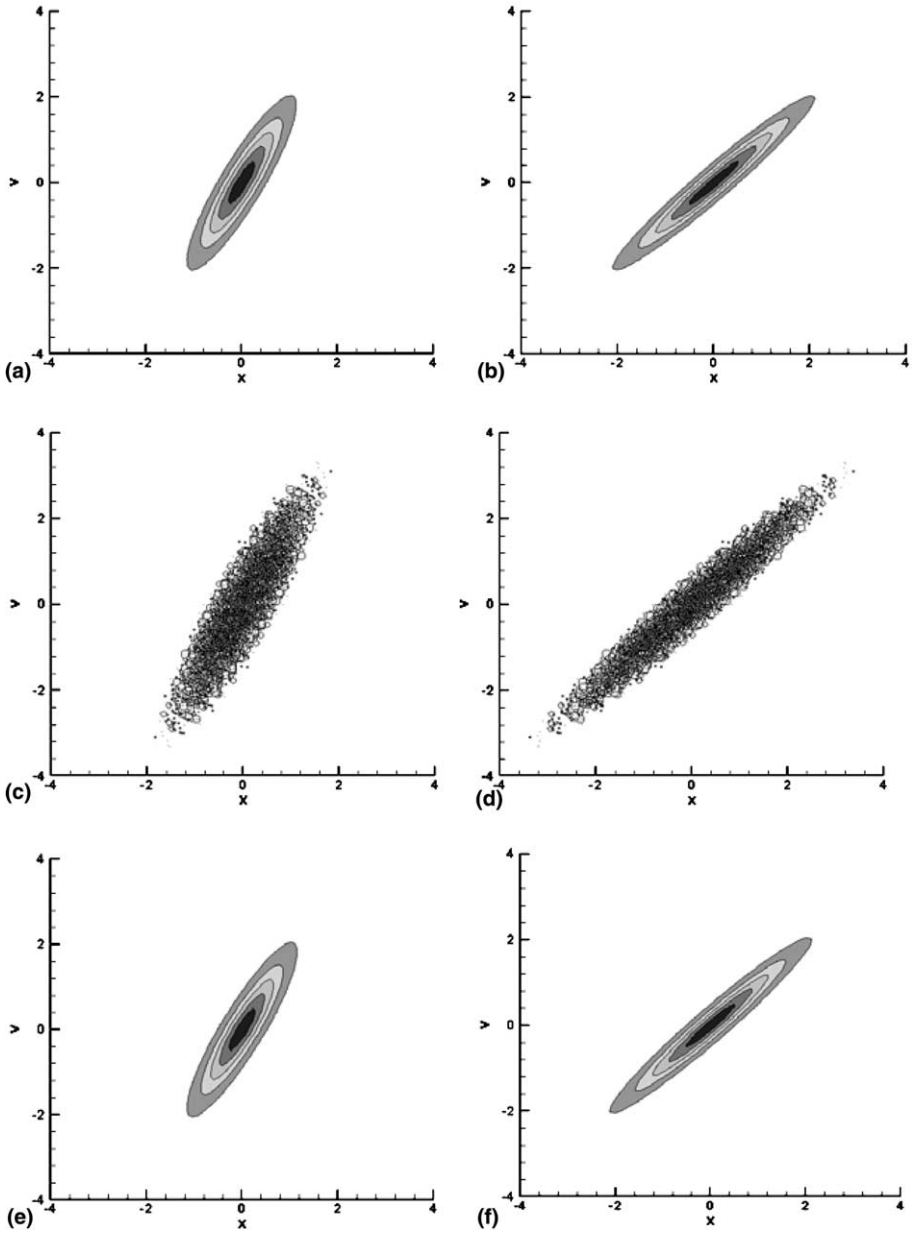

Fig. 13. The evolution of a single particle, representing a gas puff, as it evolves with its internal time parameter τ is shown in (a) $\tau = 10$ and (b) $\tau = 20$. In (c) and (d) are the results of a run starting from the same initial particle now allowed to fragment in both x and v_x until the particles become roughly 21,000 times smaller than the original. Shown in (e) and (f) are the corresponding distributions from superposition of the individual distributions within each particle.

continue to stretch as each particle's τ continues to evolve with simulation time t. Energy is conserved to machine precision.

For comparison, we also show in Fig. 13 the original particle as it evolves with increasing τ without fragmentation in (a) and (b), effectively giving the analytic solution. We compare these distributions from

Table 2

Time step	Total number of particles	Particles generated
0	1	16
1	17	272
2	289	4112
3	4401	13,616
4	18,017	2960
5	20,977	0
15	20,977	0
20	20,977	0

Table 3

Time step	Particles		
	Total	Generated	Merged
0	1	16	3
1	14	224	72
2	166	2360	756
3	1770	6152	1811
4	6111	2584	1699
5	6996	784	878
6	6902	592	671
7	6823	648	671
8	6800	784	736
9	6848	896	851
10	6893	784	772
11	6905	872	835
12	6942	872	844
13	6970	936	899
14	7007	952	932
15	7027	1008	1002
16	7033	1008	1011
17	7030	1024	1004
18	7050	1136	1107
19	7079	1072	1078
20	7073	1112	1087

the one CPK particle to the corresponding reconstructions by superposition obtained from the multi-particle fragmentation run shown in (e) and (f). These composite distributions are the result of summing the contribution of each particle, shown in (c) and (d), on a grid in v_x, x phase space that has 253 bins in velocity and 225 bins (centered on the stringer locations) in x.

The distributions should be identical at each time. The peak of the original particle, 39.443, remains constant, as its internal time is incremented, as shown in Fig. 13(a) at $t = 10$ and (b) at $t = 20$. The multi-particle distributions, shown in (e) and (f), have peak values that are slightly larger, 40.942, at $t = 10$ and, 41.059, at $t = 20$. There are several sources of this growth. Part of this growth is accounted for by the coarse grid in which we build the distribution, some is due to round off in superposing the error function contributions of 20,000 + small particles, and there is still the slight tendency for the evolved distribution to grow due to the small systematic error made at each fragmentation. Recall that this error, less than 0.5% for each individual fragmentation, is apparent when reassembling the fragmented particle immediately after fragmentation. Energy, momentum, and mass are conserved to round off.

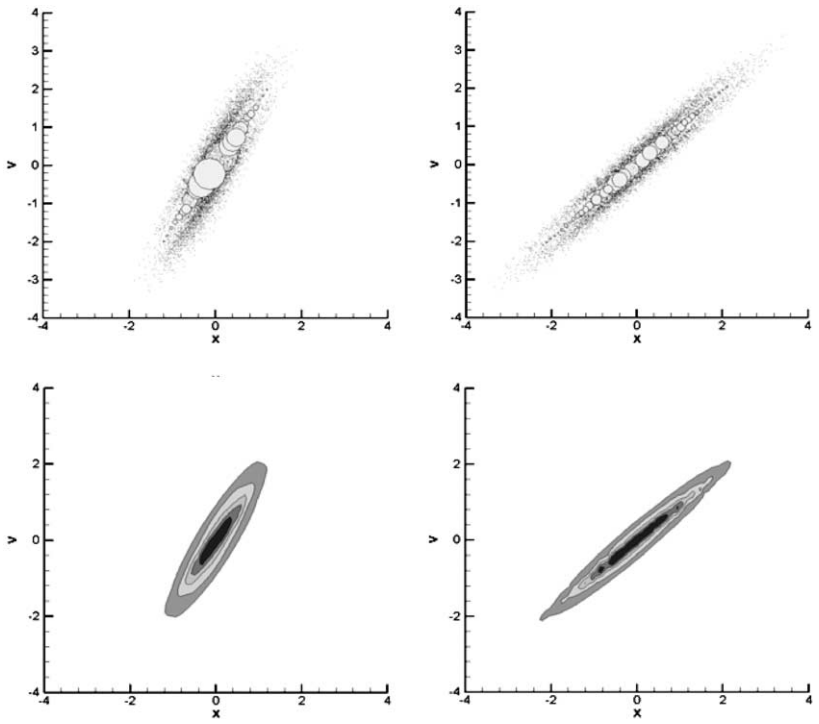

Fig. 14. The evolution of a single particle, representing a gas puff, as it evolves with fragmentation and now merging. The bulk of the distribution is now carried by larger particles, giving some indication of the economy we expect from merging. The noticeable asymmetry in the early particle disposition is a result of the initial state having only one particle and the large core particles that overtake and consume the small, slower particles that precede them in the expansion. The initial particle peak was 39.443, which grows, due to the merging, to 44.963 and 49.247 on the bottom left and right, respectively. Here we have used $effWd = 1.2$ and $effVt = 1.2$.

We next consider the same collisionless expansion but now allow merging as the run progresses. The number particles, for a few times during the course of the run, are given in Table 3. Displayed are the number of particles that exist at the start of the indicated time step followed by the number that are created by fragmentation and the number that are eliminated by merging during that step. Notice, the fragmentation rate falls off as particles become too small to fragment. The overlap parameters are $effWd = 1.2$ and $effVt = 1.2$.

In Fig. 14 are the particle phase spaces and distribution functions that result from this run. While the particles shown in both Figs. 13 and 14 are scaled according to their weight, the particles in Fig. 14 are scaled up an additional factor of 50. Thus the large particles in the middle of Fig. 14 on the upper left and right are much bigger than those in Figs. 13(c) and (d). The merged distribution is more peaked than the insignificant growth found using fragmentation alone. With merging, however, we expect some growth in the peak of the distribution due to moment conservation for pairs of particles that are co-located in phase space. We expect to lose some knowledge of the distribution during the merging process. One of the ways this materializes is in the peaking of the distribution (see Section 2.5).

To determine some measure of sensitivity to the overlap parameters, we now increase the effective particle size to enhance merging. Increasing the acceptable particle width and thermal parameters to $effWd = 1.5$ and $effVt = 1.5$, we find, as shown in Table 4, this further reduces the number of particles in the run and it decreases the peaking of the distribution function, shown in Fig. 15. Research is ongoing to understand the interaction of these parameters and to judge whether this or some other algorithm is more appropriate.

Table 4

Time step	Particles		
	Total	Generated	Merged
0	1	16	4
1	13	208	120
2	101	1376	669
3	808	2624	1027
4	2405	1328	734
5	2999	768	651
6	3116	832	683
7	3265	776	684
8	3357	800	713
9	3444	848	759
10	3533	872	791
11	3614	880	822
12	3672	936	861
13	3747	888	852
14	3783	1000	953
15	3830	976	944
16	3862	1088	1046
17	3904	1072	1059
18	3917	1168	1117
19	3968	1144	1124
20	3988	1256	1222

3.2. The Sod problem

The Sod problem [22] is a traditional shock tube problem that consists of a semi-infinite fluid on the left with density $\rho_{\text{left}} = 1$ and temperature $T_{\text{left}} = 1$ separated at $t = 0$ by a membrane from the semi-infinite region on the right that has a lower density $\rho_{\text{right}} = 0.125$ and temperature $T_{\text{right}} = 0.1$ (see Fig. 16(a)). At $t = 0$, the membrane breaks and the fluid moves towards the right and forms a traditional shock front, a contact discontinuity, and a rarefaction wave. Fig. 16(b) is the result of a 1-D Eulerian fluid computation.

The initialization of this problem in CPK is straightforward. This particular run was also made with 225 equally spaced stringer points on a mesh that extends, in dimensionless units in the code, from $x\min = 0.0$ to $x\max = 6000.0$. We used a time step of $\Delta t = 0.025$. For the high density and temperature on the left, we initialized 1000 particles with $W_{dx} = 0.05$ and $V_{tx} = 1.0$. An additional 1000 particles were used on the right with weights reduced by a factor of 8 and thermal velocities are reduced by a factor of the square root of 10, to get the appropriate reduction in density and pressure on the right. We then fragment in space some of the particles nearest the interface on the left side and discard those pieces that are generated on the right side of the interface. In this way we "sharpen" the initial interface by reducing the spatial extent of some of the particles nearest the interface. Several iterations of this process sharpen the interface and, here, give a net increase of five particles at the start of the time stepping procedure. Some of these particles are visible in Fig. 17. The run proceeds for 100 time steps, beginning with 2005 total particles.

As the simulation begins, each particle is fragmented in both space and velocity to "probe" for emerging features. In most regions, these probe particles merge with their neighbors on the left and the right, resulting in no net change to the configuration. At the interface an emerging feature is "discovered"; the flux of mass and energy from the left is unbalanced by the flux from the right, as is evident in Fig. 18.

The overlap parameters for merging have strong impact on the course of the run. In the case presented in Fig. 18, the particle count is immediately increased by 4008 as a result of x-fragmentation and then an additional 8004 from v-fragmentation. The subsequent merging eliminates 12,928 particles, leaving only

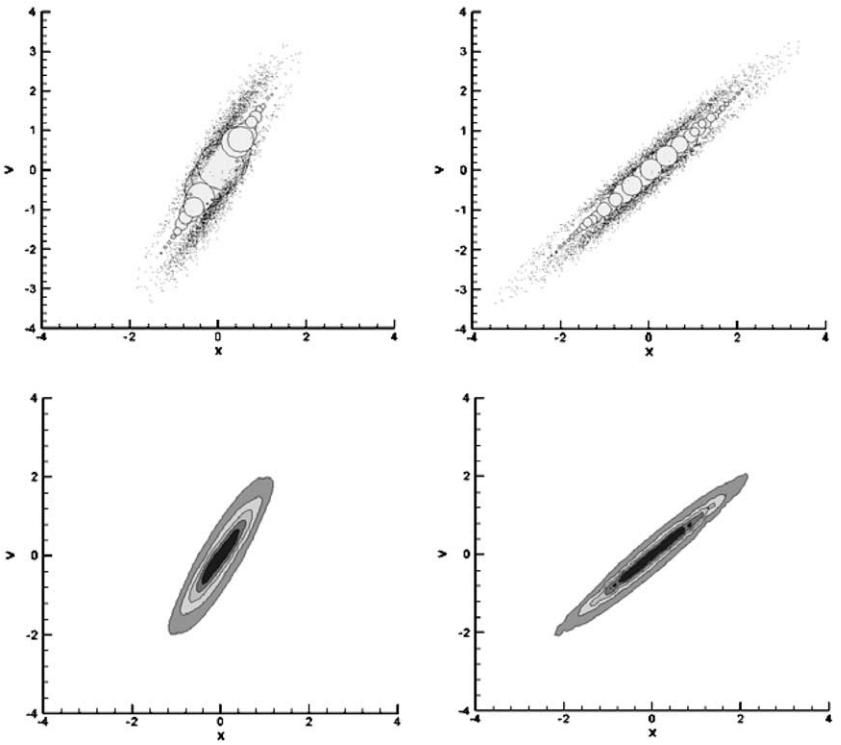

Fig. 15. The gas puff expansion of Fig. 14 with new merging criteria to gauge sensitivity. Here we have increased the aggressiveness of the merging process by decreasing the amount of overlap required for a particle merge. Here we have used $effWd = 1.5$ and $effVt = 1.5$. The particle number decreases by roughly a factor of 2 with little loss of distribution detail. The initial particle peak grows less, now to 43.884 and 46.338 on the bottom left and right, respectively.

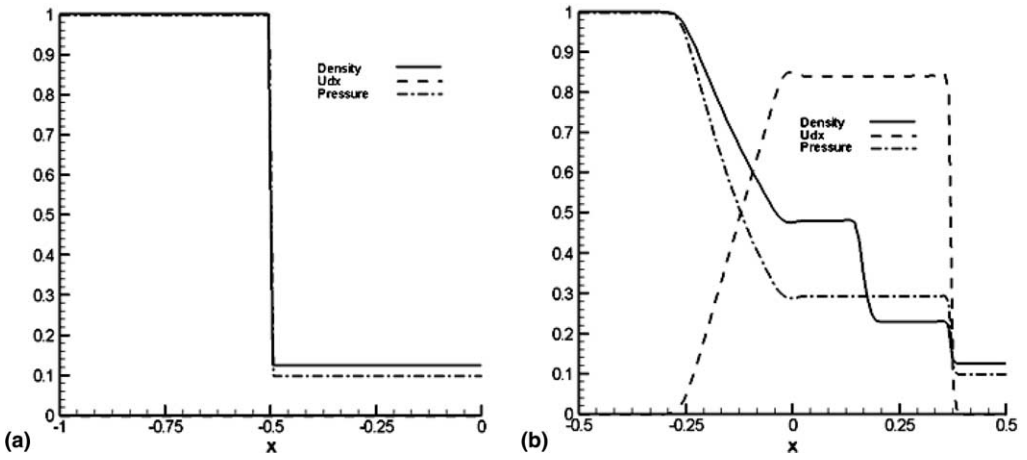

Fig. 16. An Eularian fluid simulation of the Sod shock tube problem. On the left (a) is the $t = 0$ configuration consisting of a semi-infinite fluid with density $\rho_{\text{left}} = 1$ and temperature $T_{\text{left}} = 1$ separated at $t = 0$ by a membrane from a lower semi-infinite region with density $\rho_{\text{right}} = 0.125$ and temperature $T_{\text{right}} = 0.1$. For $t > 0$, the membrane is broken and the fluid moves towards the right (b) and forms (from right to left) a shock, a contact discontinuity, and a rarefaction wave.

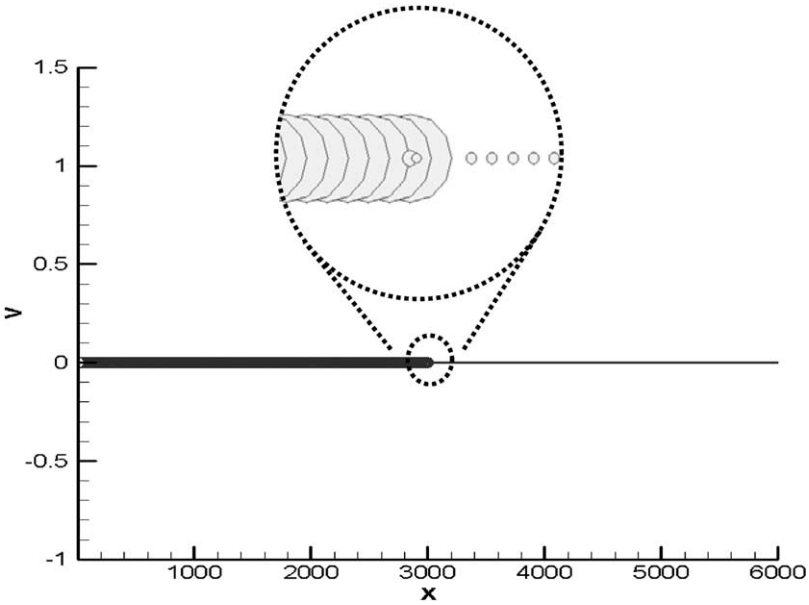

Fig. 17. The initial CPK particle configuration for the Sod problem. The initial configuration consists of 1005 appropriately weighted particles on left side of the interface and 1000 on the right. The insert is a magnification of the discontinuity showing a few of the X-fragmented particles that sharpen the discontinuity. Particle plotting sizes are proportional to particle weight.

1089 to start the second time step. After the initial transients in particle number, a typical time step starts with roughly 1500 CPK particles, increases by ~2900 due to x-fragmentation, adds ~2400 more due to v-fragmentation, and then loses ~5300 to merging. The entire run takes about 20 s on a 2 GHz Pentium, including diagnostics (expensive due to exponential evaluations). The merging overlap parameters are $effWd = 6$ and $effVt = 5$. The fragmentation constraints are that the particle must be bigger than these minimum values, $W_8 = 0.000125$, $W_{dx} = 0.0001$, $V_{tx} = 0.001$, before a particle can be fragmented. Further, we require that $W_{dx} > \Delta t V_{tx}$ to x-fragment and $W_{dx} < \Delta t V_{tx}$ to v-fragment.

A crucial measure of our success in simulating the Sod problem is that the densities and velocities must agree with theory or, in this case, the fluid calculation. Shown in Fig. 19 is a superposition of the Eulerian fluid and a density obtained with a piecewise linear interpolation of CPK particle data to give a density evaluated on each of the particle stringer locations. The code is insensitive to the number of particles and insensitive to Δt step so long as $\Delta t V_{tx} < W_{dx}$. For larger $effVt > 10.0$, merging is much more aggressive, the fast particles are merged too readily, resulting in a gradual reduction in peak velocity to the right. For lower $effVt$, for example $effVt = 2$, the physics is preserved but the particle number slowly increases to memory limits with a rate that increases as $effVt$ becomes smaller.

The discontinuities in density need to be better resolved. The lack of resolution evident here is a result of aggressive merging that produces particles with large W_{dx}s that washout the discontinuity. Further research is underway to detect these discontinuities and inhibit merging in these areas.

To evaluate the sensitivity of the result to the merging parameters, we present particle plots for a case ($effVt = 3$) with reduced tendency to merge. We find, in Fig. 20(a), a greater number of particles than in the corresponding case Fig. 18(f). In (b) is the same configuration and time as (a) but now the particle size represents the particle's spatial width W_d. In (c) the particle's size is proportional to the particle's thermal velocity V_t. From (a) we can deduce that hotter gas on the right of the contact discontinuity is represented by both a larger kinetic spread and hotter individual macro-particles as seen in (c). Comparing (b) and (c) it

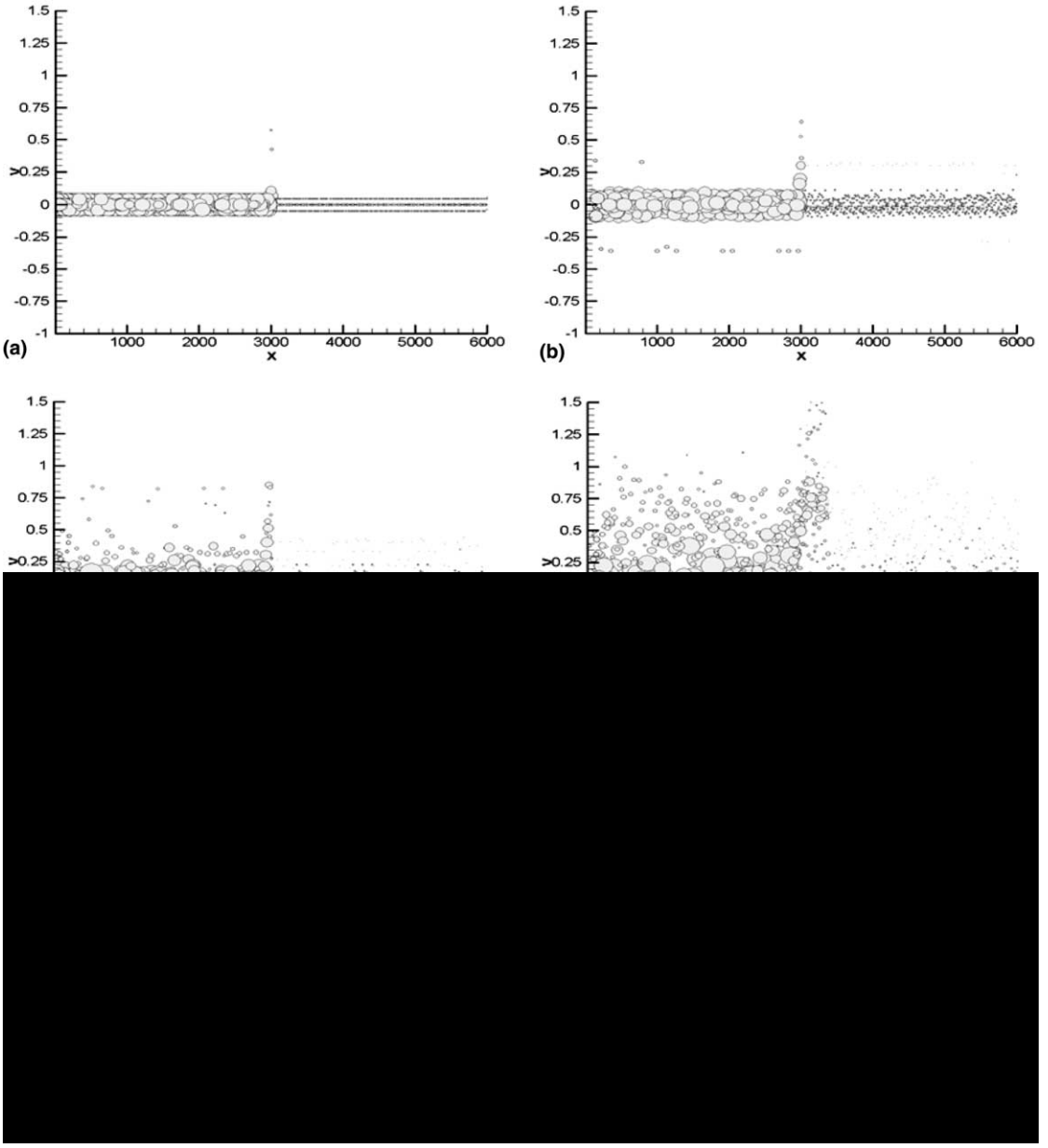

Fig. 18. Time evolution of CPK particles modeling the Sod problem. Shown are the particle configurations after: (a) 1 Δt, (b) 2 Δt, (c) 5 Δt, (d) 20 Δt, (e) 40 Δt, and (f) 100 Δt. Particle sizes are proportional to particle weight. The contact discontinuity (where the density drops and the temperature increases) is evident in the lower right panel ($x \sim 4000$).

is obvious that the ensemble averages of W_d and V_t remain correlated, due in this case to the fragmentation constraints that require x-fragmentation of particles with large W_d and v-fragmentation of particles with large V_t.

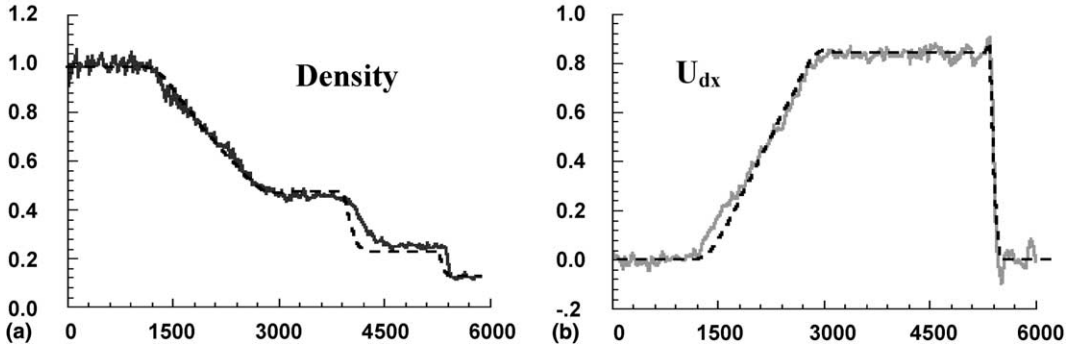

Fig. 19. CPK density (a) and drift velocity (b) compared to the Eulerian fluid calculation (shown in dashed black lines). One hundred points are used in the fluid calculation compared to 225 equally spaced stringer points in the CPK calculation. The most obvious discrepancy is the reduced flow velocity on the right that causes disagreements in the density profiles in the figure on the left.

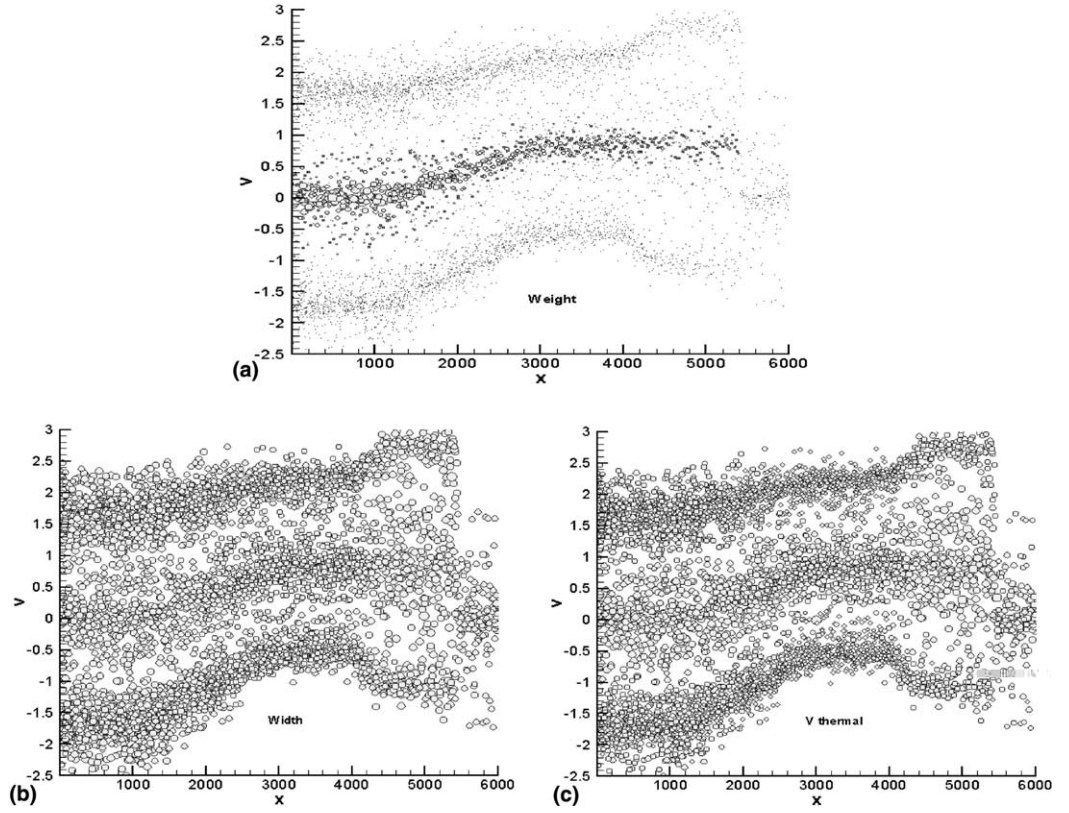

Fig. 20. CPK particle phase space, with less aggressive merging ($effVt = 3$), is shown for comparison with the run shown in Fig. 18 with ($effVt = 5$). In (a) is the CPK phase-space configuration with particle size again proportional to macro-particle weight. In (b) is the same configuration as (a) but now the particle size represents the particle's spatial width W_d. In (c) the particle's size is proportional to the particle's thermal velocity V_t. Note the change in particle parameters across the contact discontinuity.

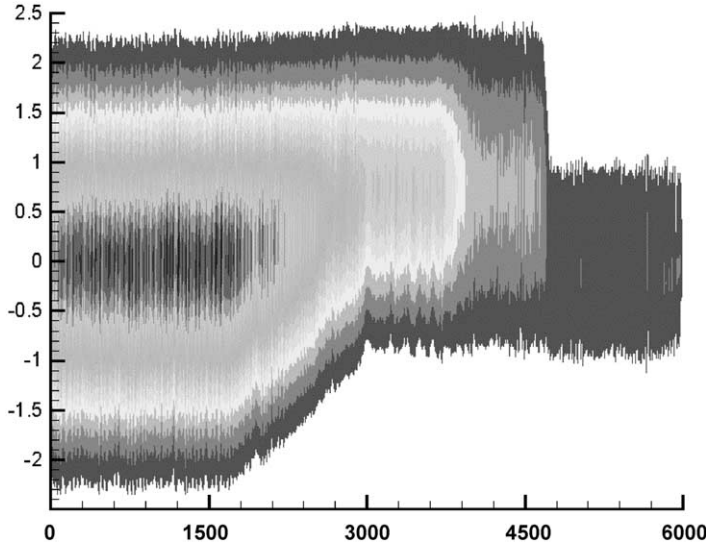

Fig. 21. The composite distribution made from the parameters of the particle representations shown in Fig. 20(a). Note the change in the distribution on opposite sides of the contact discontinuity around $x = 3900$.

Finally, we reconstruct a full distribution function $f(x, v_x, t = 100\Delta t)$ from the particles. Shown in Fig. 21 are contours of the distribution that results when we superpose the contributions of all particles using the individual distributions that characterize each particle.

4. Conclusions and future work

We have described the basic particle and a sequence of operations for use in a new type of "smart PIC" algorithm, intended to bridge the gap between Eulerian fluid regimes and kinetic regimes for plasma or rarified gases. We have enlarged the scope of PIC by using a particle format that consists of grouping real particles into fluid-like macro-particles that have Gaussian shapes in space and Maxwellian profiles in velocity. The simulation concept, called CPK for Complex Particle Kinetics, is to aggressively fragment these particles to probe for emerging features in phase space and to merge particles if interesting features fail to materialize. Essential to this concept is the ability to fragment macro-particles without adding new features to the distribution function and to merge particles, for economy, so that the interesting macroscopic moments are preserved. Fragmentation preserves the kinetic capabilities of PIC; merging dramatically shrinks the number of particles in non-kinetic or collisional regions.

Time evolution is modeled by a combination of the Lagrangian motion of each of these macro-particles and internal evolution within each individual macro-particle. An analytic term is added to each particle's shape that represents internal evolution consistent with the collisionless, free-streaming of each macro-particle. Collision-dominated, γ-law gas internal evolution is also developed to define the opposite limit of collisionality. In collision-dominated regimes, merging becomes more effective—leading to fewer Lagrangian particles that begin to act much as nodes in Free-Lagrangian hydrodynamics.

A key part of the concept is that the physics unfolds as nature intends. The only connection between neutral particles is through collisions. The gradient of pressure is never computed and the "mesh" enters only in a non-fundamental way as a means to facilitate evaluating particle phase space "overlap" during merging.

We have performed preliminary tests on these concepts. Simple collisionless free expansions using fragmentation and merging show the desired tendencies to form a few relatively large particles in the bulk of the distribution while retaining a few small, cold particles to probe for interesting features. Collision-dominated tests have been carried out on the Sod shock tube problem. These tests have verified the algorithm's ability to detect and nurture emerging features. Further, the algorithm's ability to recover the essential physics in the Eulerian fluid limit without use of an explicit pressure gradient verifies that the concept of probing and merging will work in the collisional limit and that there is no need for a mesh that does more than facilitate the particle merging operation. We are optimistic that these features may eliminate mesh imprinting.

Efforts are now underway to make the algorithm multi-dimensional and to investigate partially collisional concepts to couple with adaptive merging concepts.

Acknowledgements

The author acknowledges many fruitful discussions with D.J. Larson over the latter stages of this work. In addition, G. Zimmerman was instrumental in the development of the internal dynamics for the collision-dominated regime. The concepts of fragmenting and merging simulation particles, common to both CPK and the earlier GaPH model [1], have their genesis in conversations with GaPH coauthor W.B. Bateson.

This work was performed under the auspices of the US Department of Energy by the University of California, Lawrence Livermore National Laboratory under Contract No. W-7405-Eng-48.

References

[1] W.B. Bateson, D.W. Hewett, Grid and particle hydrodynamics: beyond hydrodynamics via fluid-element particle-in-cell, J. Comp. Phys. 114 (1998) 358.
[2] F.H. Harlow, PIC and its progeny, Comp. Phys. Commun. 48 (1988) 1.
[3] B.M. Marder, GAP-a-PIC-type fluid code, Math. Comput. 29 (130) (1975) 434.
[4] C.K. Birdsall, A.B. Langdon, Plasma Physics via Computer Simulation, McGraw-Hill, New York, 1985.
[5] R.W. Hockney, J.W. Eastwood, Computer Simulation Using Particles, McGraw-Hill, New York, 1981.
[6] D.W. Hewett, Low-frequency electromagnetic (Darwin) applications in plasma simulation, Comp. Phys. Commun. 84 (1994) 243.
[7] S. Rudman, S.G. Rubin, Hypersonic viscous flow over slender bodies with sharp leading edges, AIAA J. 6 (1968) 1883.
[8] P.J. Roache, Fundamentals of Computational Fluid Dynamics, Hermosa, Albuquerque, 1998.
[9] T. Takizuda, H. Abe, A binary collision model for plasma simulation with a particle code, J. Comp. Phys. 25 (1977) 205–219.
[10] C.K. Birdsall, Particle-in-cell charged-particle simulations, plus Monte Carlo collisions with neutral atoms, PIC-MCC, IEEE Trans. Plasma Sci. 19 (2) (1991) 65–85.
[11] P.W. Rambo, J. Denavit, Interpenetration and ion separation in colliding plasmas, Phys. Plasmas 1 (12) (1994) 4050.
[12] P.W. Rambo, R.J. Procassini, A comparison of kinetic and multifluid simulations of laser-produced colliding plasmas, Phys. Plasmas 2 (1995) 3130.
[13] M.E. Jones, D.S. Lemons, R.J. Mason, V.A. Thomas, D. Winske, A grid-based coulomb collision model for PIC codes, J. Comp. Phys. 123 (1996) 169–181.
[14] M.L. Hudson, T.J. Bartel, Direct simulation Monte Carlo computation of reactor-feature scale flows, JVST A 15 (3) (1997) 559.
[15] M.J. Berger, P. Colella, Local adaptive mesh refinement for shock hydrodynamics, J. Comp. Phys. 82 (1989) 64.
[16] C.W. Hirt, A.A. Amsden, J.L. Cook, An arbitrary Lagrangian–Eulerian computing method for all flow speeds, J. Comp. Phys. 135 (1974) 203.
[17] J.P. Monohan, Smoothed particle hydrodynamics, Ann. Rev. Astron. Astrophys. 30 (1992) 543.
[18] G.G.M. Coppa, G. Lapenta, G. Dellapiana, F. Donato, V. Riccardo, Blob method for kinetic plasma simulation with variable-size particles, J. Comp. Phys. 127 (1996) 268.
[19] G. Zimmerman, private communication.
[20] D.J. Larson, A coulomb collision model for PIC plasma simulation, J. Comp. Phys. 181 (2003) 123–138.
[21] R.H. Miller, M.R. Combi, A coulomb collision algorithm for weighted particle simulations, Geophys. Res. Lett. 21 (1994) 1735.
[22] G.A. Sod, Numerical Methods in Fluids Dynamics, Cambridge, 1986.